



Evolution and exhumation of intrusive rocks associated with the Naozhi porphyry–epithermal system, NE China

Yang Liu^{1,2,3} · Jinggui Sun^{1,3} · Pete Hollings² · Barry P. Kohn⁴ · Matthew J. Brzozowski⁵

Received: 14 March 2023 / Accepted: 29 October 2023 / Published online: 13 December 2023
© The Author(s), under exclusive licence to Springer-Verlag GmbH Germany, part of Springer Nature 2023

Abstract

The Naozhi deposit of northeast China comprises intermediate-sulfidation epithermal-style veins and subeconomic, porphyry-style Cu mineralization hosted by dioritic to granitic plutons, which formed at ca. 130 Ma. These intrusive phases were fed by magmas that ponded at mid- to upper-crustal levels and were finally emplaced at <0.6 kbar based on amphibole geobarometry. The magmas were moderately oxidized ($\Delta\text{NNO} = 0.35$ to 2.21; with NNO being the nickel–nickel–oxide buffer) and water-rich (mostly >4 wt. %), and likely experienced a relatively prolonged evolution in the shallow crust rather than at depth. Magma devolatilization and fluid exsolution at shallow-crustal levels lead to decreases in both oxygen fugacity ($\log f\text{O}_2 = -10.96$ to -14.13) and water content (6.53 to 2.26 wt. %) at <2.5 kbar pressures. Thermochronological data of zircon and apatite, thermal history modeling, and geological preservation record complex time–temperature histories of the mineralized intrusive rocks, from the cooling of the parent magma itself through burial by younger volcanic rocks to protracted erosion with time. It is estimated that <2 km of pre-mineralization material was removed from the top of the Naozhi magmatic–hydrothermal system from the Early Cretaceous to present. A 108 ± 2 Ma volcanic event possibly tilted the hydrothermal system, but buried the ores, protecting them from extensive erosion.

Keywords Mineral geobarometer · Low-temperature thermochronology · Physicochemical states · Exhumation history · Naozhi porphyry–epithermal system

Introduction

Subduction zones are natural factories in which numerous hydrothermal deposits are formed (Richards 2003; Cooke et al. 2006; Evans and Tomkins 2011; Wilkinson 2013),

particularly Cu and Mo porphyry deposits (Sillitoe 2010). Porphyry Cu deposits (PCDs) tend to form at depths of 2–5 km in subduction and post-collisional environments (Seedorff et al. 2005; Sillitoe 2010), whereas epithermal deposits form at shallower depths of <1.5 km (Hedenquist et al. 2000; Simmons et al. 2005). These two deposit types can be vertically and laterally telescoped (Sillitoe and Hedenquist 2003; e.g., Bingham Canyon, Utah; Tomlinson et al. 2021; Maricunga Belt, Northern Chile; Muntean and Einaudi 2001; Hollings and Cooke 2005; Mankayan district, Philippines; Chang et al. 2011; Onto, Indonesia; Burrows et al. 2020; Zijinshan, China; Chen et al. 2019). In these settings, the economic porphyry Cu ores are generally buried or poorly exposed, where the epithermal mineralization is well preserved, e.g., Tavua, Fiji (a world-class epithermal adularia–sericite gold deposit; Eaton and Setterfield 1993) where porphyry subeconomic copper–gold mineralization was superimposed vertically by acid sulfate epithermal mineralization, evolved to lateral adularia–sericite epithermal mineralization. In some telescoped deposit cases, epithermal mineralization is considered to be the near-surface

Communicated by Gordon Moore.

✉ Jinggui Sun
sunjinggui@jlu.edu.cn

- ¹ College of Earth Sciences, Jilin University, Changchun 130061, China
- ² Geology Department, Lakehead University, Thunder Bay, ON P7B 5E1, Canada
- ³ Key Laboratory of Mineral Resources Evaluation in Northeast Asia, Ministry of Land and Resources of China, Changchun 130061, China
- ⁴ School of Geography, Earth and Atmospheric Sciences, University of Melbourne, Victoria 3010, Australia
- ⁵ British Columbia Geological Survey, 1810 Blanshard Street, Victoria, BC V8T 4J1, Canada

expression of porphyry copper hydrothermal system (Eaton and Setterfield 1993; Hedenquist et al. 2000; Sillitoe and Hedenquist 2003; Sillitoe 2010), and therefore, provides guide to economically important deep PCDs (e.g., Chang et al. 2011). However, the ability to accurately quantify preservation potential of ore deposits remains challenging.

The Naozhi deposit of northeastern China contains intermediate-sulfidation (IS) epithermal-style veins and subeconomic porphyry-style Cu mineralization within 2 km of each other, both being associated with the same Early Cretaceous (~130 Ma) calc-alkaline intrusive rocks, and is demonstrated to be a telescoped hydrothermal system (Liu et al. 2021). Despite no acid sulfate epithermal mineralization top was observed that has likely been eroded away, the Naozhi hydrothermal system is considered an analogue to the Tavua. Further understanding the preservation of Naozhi system is therefore critical for deep porphyry ore potential, which is dependent on the original depth of emplacement and the rate of post-mineralization exhumation (McInnes et al. 2005). Amphibole geothermometers are an applicable approach to effectively characterize the depth and pressure of emplacement of intrusions, which require amphibole being in equilibrium with the intruding magmas (Dahlström et al. 2022), and have been used to characterize the emplacement depth of porphyry deposits (e.g., <2 km for Batu Hijau, Indonesia; Garwin 2000). Reconstructing the post-mineralization tectonic evolution is a valid path to assess preservation potential of ore deposits (McInnes et al. 2005). Low-temperature thermochronology (LTT), such as apatite fission-track (AFT) analysis (Gleadow et al. 1986; Gallagher et al. 1998), and apatite and zircon (U–Th)/He geochronology (e.g., McInnes et al. 2005) have been extensively applied to characterize the exhumation histories of hydrothermal ore deposits (e.g., McInnes et al. 2005; Fu et al. 2010; Leng et al. 2018; Gong et al. 2021). Interpreting LTT data, however, requires significant knowledge of the geological history of the deposit, which is scarcely preserved. It is noted that much geological evidence that multiple intrusive phases related to mineralization and post-mineralization volcanic covering were well preserved at Naozhi and therefore provide key constraints on reconstructing the post-mineralization tectonic evolution. Here, we present new amphibole chemistry and LTT data (apatite fission track [AFT] and apatite and zircon (U–Th)/He [AHe and ZHe], respectively) to investigate the magmatic system and assess the preservation potential of the Naozhi hydrothermal system.

Geological setting

The Naozhi deposit is located in the southern portion of the Xingkai massif, in the eastern segment of northeast China (Fig. 1); it comprises several microcontinental massifs (e.g.,

Erguna, Xing'an, Songnen, Jimusi, and Xingkai) that amalgamated prior to the Mesozoic. This region is endowed in gold and containing numerous magmatic–hydrothermal gold deposits (Fig. 1). These gold deposits are mostly Early Cretaceous in age, with few deposits being late Paleozoic (Ren et al. 2016). According to the mineralization–alteration styles and their relationships with the intrusive rocks, these gold deposits are classified as porphyry (Early Cretaceous—Xiaoxinancha, Nongping, and Sandaogou deposits; Sun et al. 2008, epithermal (Early Cretaceous—the low-sulfidation (LS) Wufeng, Wuxingshan, Ciweigou, and Ganhegou deposits; Sun et al. 2013; the intermediate-sulfidation (IS) Naozhi deposit; Liu et al. 2021; the high-sulfidation (HS) Jiusangou, Duhuangling, Canglin, and Xingou deposits; Chai et al. 2015), and intrusion-related deposit (late Paleozoic—Yangjingou and Wudaogou deposits; Ren et al. 2016). Subduction of the Paleo-Asian plate during the Paleozoic created the basement rocks in this region (Wilde 2015). The basement rocks consists of a variety of Paleozoic metasedimentary rocks, including schist, marble, and metasandstone, as well as minor amounts of early Paleozoic amphibolite and late Paleozoic metavolcanic rocks, metaconglomerate, and metasandstone. The basement rocks were intruded by 282–253 Ma dioritic intrusions (Cao 2010) and 268–256 Ma I-type granitic stocks (Wu et al. 2011). Subduction of the paleo-Pacific and Pacific slabs under the Eurasian continent controlled the regional distribution of Mesozoic volcanic rocks and intrusive rocks and Cenozoic basalt flows. The volcanic rocks are mostly 130–100 Ma in age (Xu et al. 2013) and are spatially related to several epithermal low-sulfidation gold deposits (Fig. 1). The Mesozoic intrusive rocks are dominated by Jurassic diorite to granodiorite stocks (200–160 Ma; Xu et al. 2013) and, to a lesser degree, by 130–94 Ma dioritic to granitic stocks (Ma et al. 2017). The Cretaceous intrusive rocks are either host to or spatially close to porphyry-type and epithermal high-sulfidation and intermediate-sulfidation gold deposits (Fig. 1).

Deposit geology

The IS epithermal-style veins currently mined at Naozhi occur at the edge of the porphyry system. They have a dominantly northwest–southeast strike (Fig. 2) and have been mined to a depth of 500 m. The veins are hosted by Early Cretaceous andesite (130 ± 2 Ma; Liu et al. 2015), diorite porphyry dikes (128 ± 1 Ma; Liu et al. 2021), and a Jurassic granodiorite pluton (189 ± 1 Ma) (Fig. 3a and b). A post-mineralization dacitic pyroclastic suite, with a zircon U–Pb age of 108 ± 2 Ma (Li et al. 2020), with a preservation thickness of 1.6 km in the adjacent Yanji Basin (Shi 2008), overlies the pre-mineralization andesite and is separated from them by a 2-m thick conglomerate layer. A steep contact

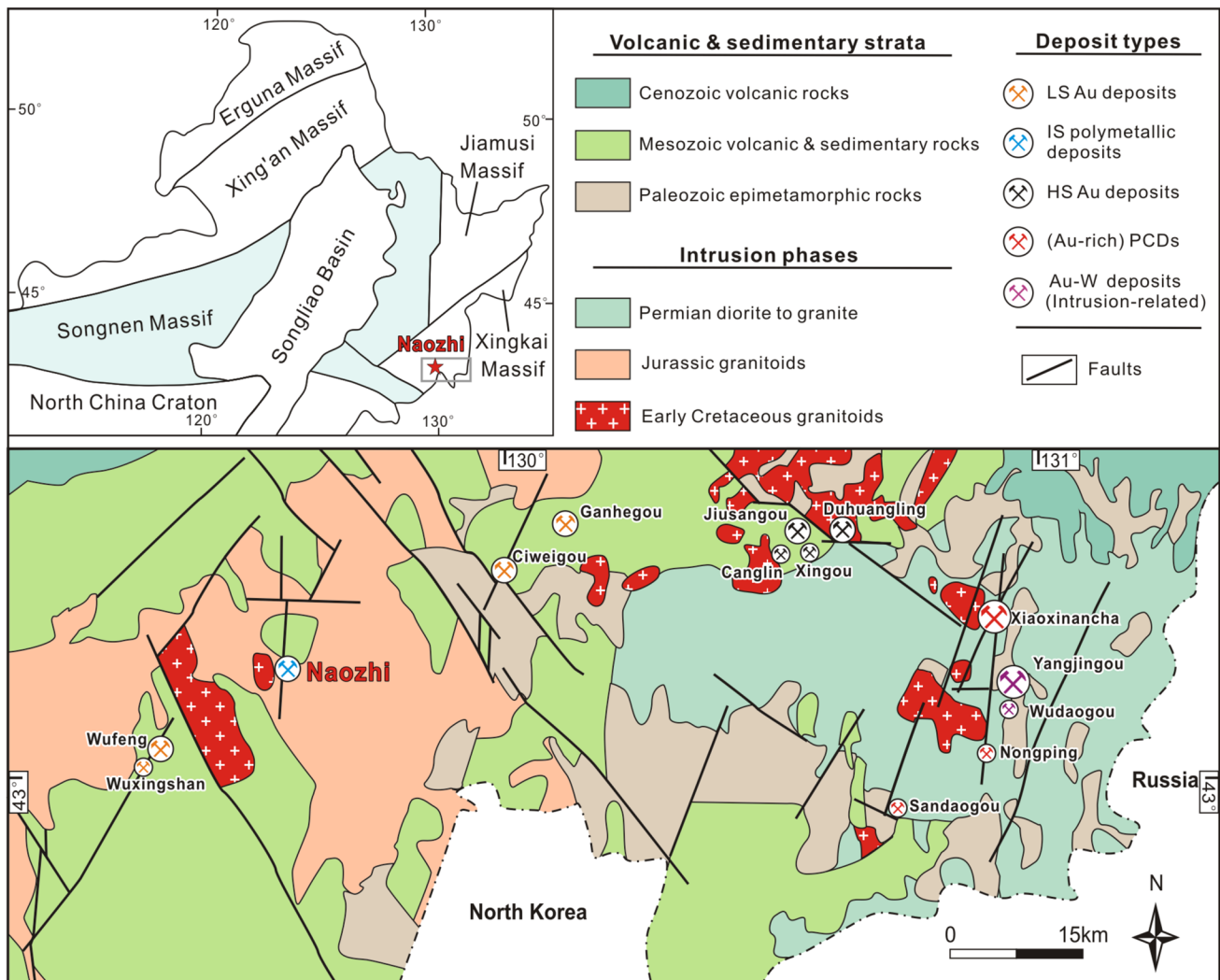


Fig. 1 Simplified geologic map of the southern Xingkai Massif showing the distribution of Mesozoic granitoid–volcanic rocks, and the location of the Naozhi district and other significant deposits (modified from Chai et al. 2015; Gu et al. 2016). Red inset (top left) shows the location of the map area in northwestern China (after Wu et al.

2011). The (Au-rich) porphyry Cu and epithermal deposits formed in the Cretaceous, whereas the Au–W deposits formed in the Late Triassic. *HS* high-sulfidation, *IS* intermediate-sulfidation, *LS* low-sulfidation, *PCDs* porphyry Cu deposits

occurs between the dacitic pyroclastic suite and andesite suite. The primary ore minerals are pyrite, chalcopyrite, sphalerite, galena, bornite, digenite, chalcocite, and electrum (Fig. 3c–f). The shallow veins are generally more economic in terms of both Cu and Au (\pm Ag), whereas the roots of the veins have higher grades of Pb and Zn. Quartz is the most common gangue mineral, with abundant late-stage carbonate minerals having formed during the waning stage of hydrothermal activity (Fig. 3a). Intense phyllic alteration centered on the veins partially to completely obscures the textural characteristics of the host rocks; replacement of rock-forming minerals and matrix by sericite, microcrystalline quartz, adularia, and pyrite is common. The intermediate argillic to propylitic assemblages comprise the distal alteration. Some

chlorite \pm epidote veins intruded the potassic alteration in the granodiorite host at depth (Fig. 3b). Precise geochronology, including zircon U–Pb dating of the andesite host (130 ± 2 Ma) and Ar–Ar dating of hydrothermal sericite (129 ± 1 Ma; Han et al. 2013) demonstrates a temporal link between the IS epithermal mineralization and the Early Cretaceous andesite.

Two kilometers northwest of the IS epithermal-style veins, disseminated chalcopyrite occurs in a weakly altered dioritic–granitic complex dated at between 129 ± 1 Ma and 126 ± 1 Ma (Liu et al. 2021). It is inferred that this intrusive complex is the core of the Naozhi porphyry system. Potassic (Fig. 4a–c) and phyllic alteration (Fig. 4d) dominates the core of the intrusive complex, but no propylitic alteration has been

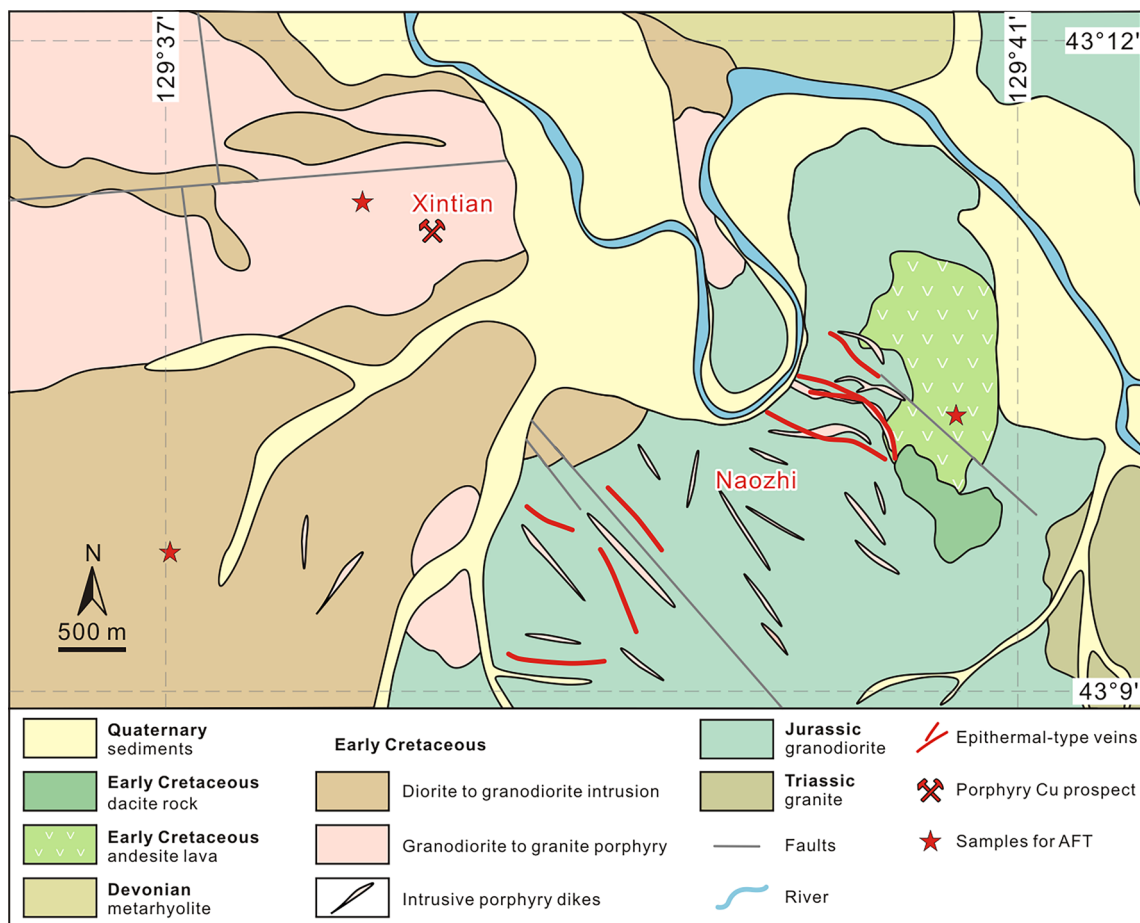


Fig. 2 Detailed geologic map of the Naozhi district, including lithologies, faults, and the locations of epithermal veins and porphyry Cu prospects, as well as the zircon and apatite sample locations. Previous

geochronological data, including zircon U–Pb and sericite Ar–Ar age data (Han et al. 2013; Liu et al. 2021) are also shown. *Zrn* zircon, *Ser* sericite

observed. Where the potassic halo occurs, rare A-type veins with wavy margins, and secondary K-feldspar, biotite, quartz, magnetite, chalcopyrite, and pyrite (Fig. 4e–f) have replaced the primary mineral assemblage of the granodiorite stock. In the mineralized phyllic zone, primary minerals of the granodiorite porphyry stock have been altered to illite, sericite, quartz, and rare chalcopyrite (Fig. 4d). Some sulfide-free quartz veinlets crosscut the early pyroxene diorite and weak sericite alteration overprints the central granite porphyry, suggesting that a fluid event postdated magma emplacement. A remarkable diversity of fluid inclusions was trapped by hydrothermal quartz in the potassic zone, including daughter-bearing (e.g., halite, anhydrite, sylvite, hematite, and magnetite) and aqueous inclusions (Liu et al. 2022), both of which are typical in PCDs (e.g., Roedder 1971).

Petrography

The intrusive complex comprises mafic to felsic stocks and equivalent dikes, with five intrusive phases having been identified by Liu et al (2021), including, from oldest to youngest, an equigranular pyroxene diorite, granodiorite, diorite porphyry, granodiorite porphyry and granite porphyry. The pyroxene diorite was intruded by a granodiorite stock; these two intrusive phases represent the pre-mineralization intrusive stage. The diorite porphyry, granodiorite porphyry, and granite porphyry represent the syn-mineralization intrusive assemblage and were emplaced into the granodiorite stock (Liu et al. 2021). The age of the intrusive complex overlaps with the Ar–Ar

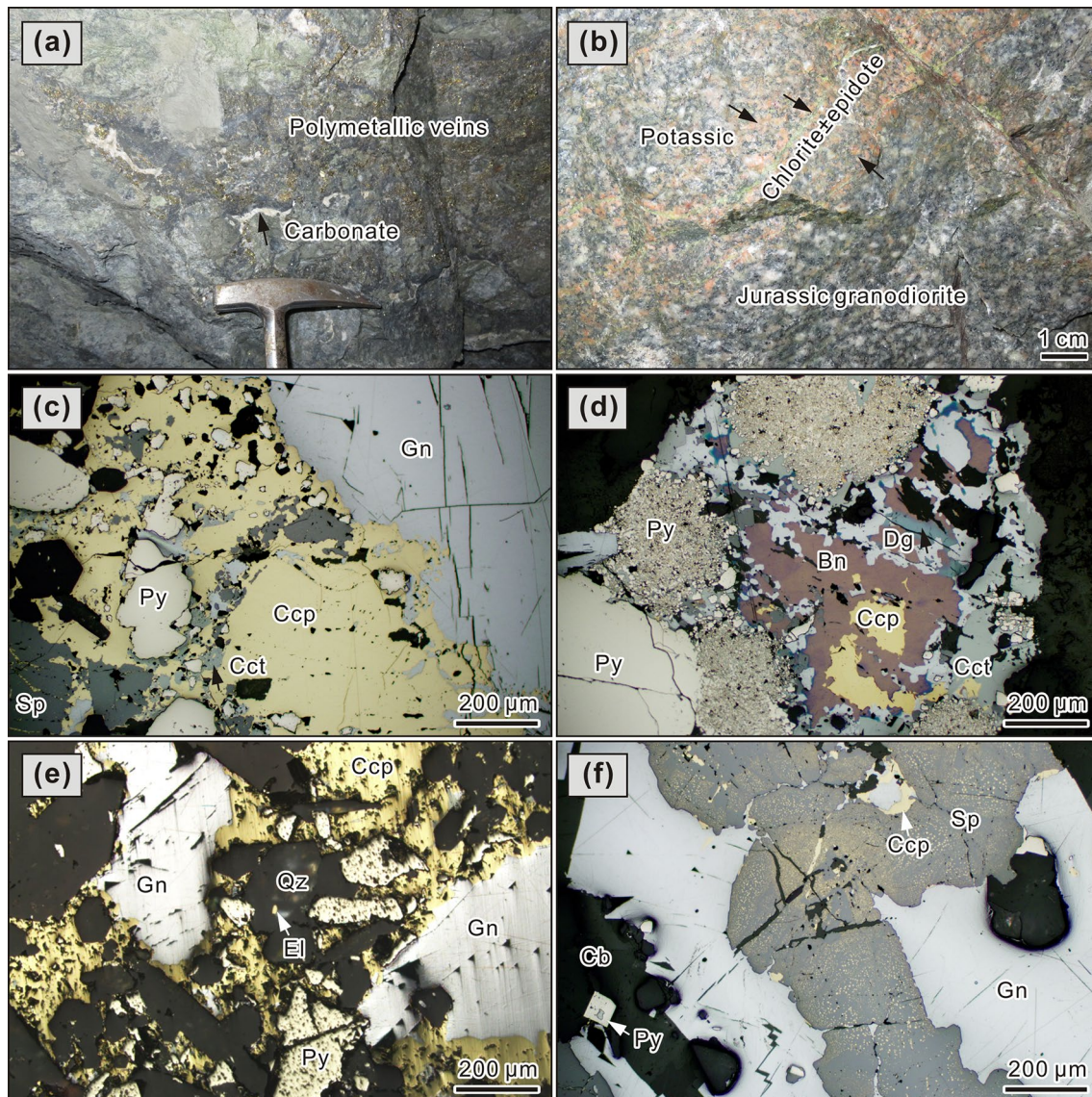


Fig. 3 Photographs and photomicrographs of epithermal-style veins and alteration in the mining tunnel at Naozhi. (a) An underground economic vein composed of sulfide and carbonate. (b) K-feldspar and chlorite ± epidote replacements of the granodiorite hosts. (c) Ccp–Cct assemblage in an epithermal-style vein, with pyrite inclusions; Chalcopyrite is replaced by the later sphalerite and galena. (d) Ccp–Cct–Dg–Bn assemblage enclosing cumulates of fine-grained pyrite coex-

isting with coarser euhedral pyrite. (e) Qtz–El assemblage interstitial to early pyrite, chalcopyrite, and galena. (f) A sulfide-rich vein composed of galena, chalcopyrite, and sphalerite. The vein has been cut by a late carbonate vein containing pyrite inclusions. *Bn* bornite, *Cb* carbonate, *Ccp* chalcopyrite, *Cct* chalcocite, *Dg* digenite, *El* electrum, *Gn* galena, *Py* pyrite, *Qz* quartz, *Sp* sphalerite

age (129 ± 1 Ma; Han et al. 2013) of hydrothermal sericite from epithermal-style veins in the phyllic zone.

The pyroxene diorite comprises plagioclase (50–60 vol. %, 0.5–2.0 mm long), hornblende (20–30 vol. %, 0.3–1.5 mm long), biotite (10–20 vol. %; 0.2–1.0 mm long), trace quartz (<2 vol. %; 0.1–0.2 mm long) and clinopyroxene (<1 vol. %; 0.1–0.2 mm long), and accessory apatite, zircon, and magnetite (Fig. 5a–c). The clinopyroxene is partially to completely replaced by actinolite and/or biotite, with magnetite occurring as inclusions; the clinopyroxene, therefore, largely

occurs as relicts (Fig. 5a and b). The replacement reaction of clinopyroxene + $H_2O \rightarrow$ actinolite is suggestive of a water-oversaturated state in the magmatic–hydrothermal environment. Primary hornblende occurs as cumulates (Fig. 5b) and euhedral grains (Fig. 5c), but they are not compositionally zoned. The former occasionally encloses inclusions of round plagioclase, together with biotite, is interstitial among those euhedral plagioclase grains, suggesting a subsolidus origin (Fig. 5b and c). Euhedral hornblende occurs with euhedral plagioclase, suggesting that they are in equilibrium (Fig. 5c).

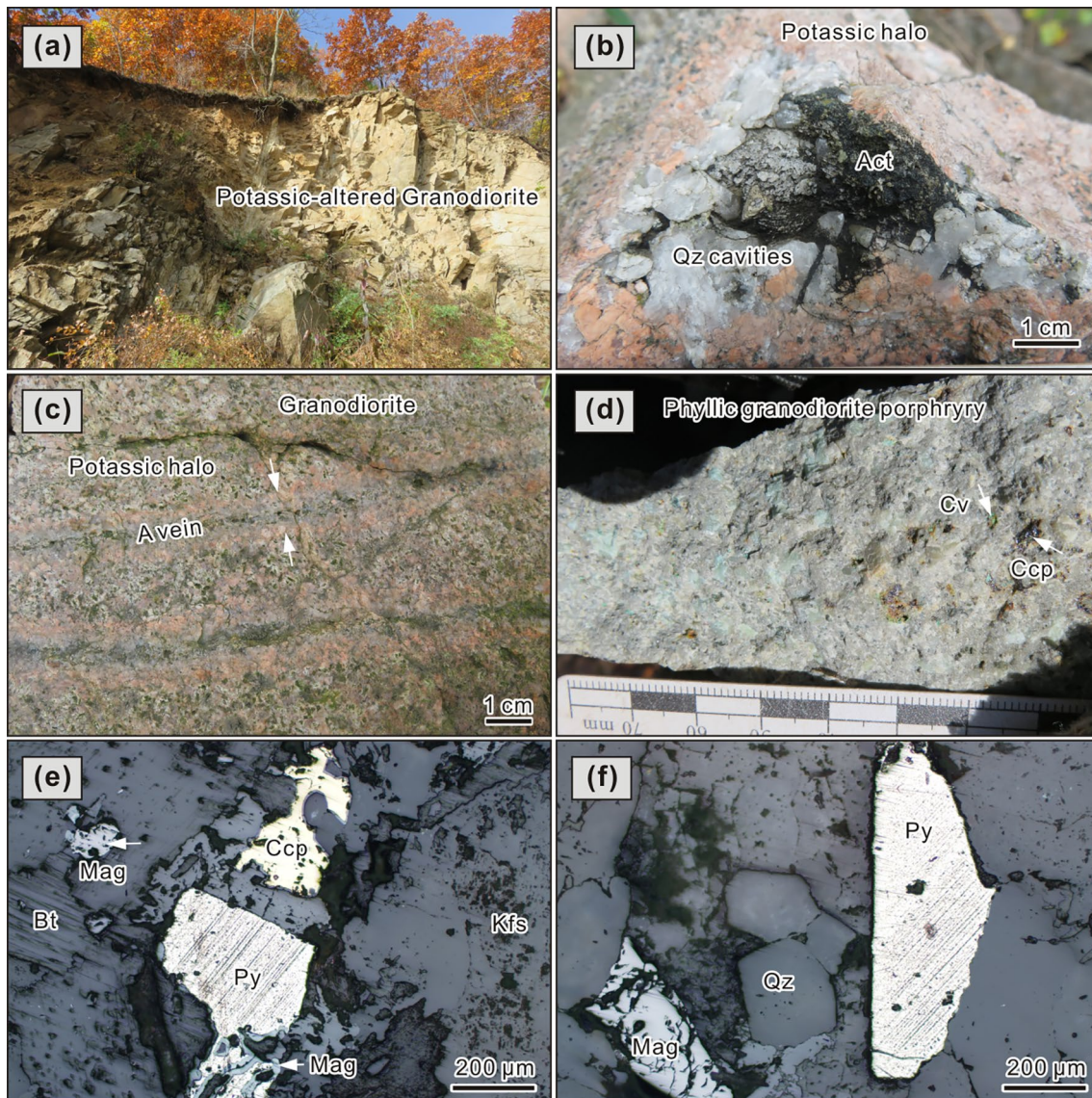


Fig. 4 Photographs and photomicrographs of porphyry-style alteration and mineralization at Naozhi. **a** Potassic-altered granodiorite exposed at surface. **b** Potassic halo, with a marginal zone comprising K-feldspar and a central zone comprising quartz and actinolite filling in open spaces. **c** Potassic-altered granodiorite, with the groundmass largely replaced by K-feldspar, and abundant secondary biotite and magnetite. The sample has been crosscut by wavy A-type quartz–bio-

tite–pyrite–chalcopyrite–magnetite veins. **d** Phyllic-altered granodiorite porphyry comprising sericite–illite–chalcopyrite; covellite formed as a result of weathering. **e** A-type vein comprising biotite, K-feldspar, magnetite, pyrite, and chalcopyrite. **f** Quartz–magnetite–pyrite association in a A-type vein. *Act* actinolite, *Bt* biotite, *Ccp* chalcopyrite, *Cv* covellite, *Mag* magnetite, *Py* pyrite, *Qz* quartz

The granodiorite mainly contains plagioclase (50–60 vol. %, 0.2–2.5 mm long), quartz (15–20 vol. %; 0.3–1.5 mm long), amphibole (~5 vol. %; 0.3–2.0 mm long), and biotite (~5 vol. %; 0.4–1.2 mm long). Most of the amphibole and biotite are euhedral (Fig. 5d), and are surrounded by quartz and some feldspar, suggesting that they formed early in the crystallization sequence. Fractures in rhombic amphibole grains (high-Al) are filled by opaque minerals (Fig. 5d), whereas unfractured tetragonal and rhombic amphibole grains (low-Al) occur with euhedral plagioclase (Fig. 5e).

Anhedral quartz grains occur in the space between amphibole and plagioclase, and occasionally partially replace the amphibole and biotite crystals; this quartz is interpreted to result from late-stage crystallization at subsolidus conditions.

The diorite porphyry contains phenocrysts of amphibole (20–30 vol. %; 0.2–1.5 mm long), plagioclase (15–20 vol. %; 0.2–2.0 mm long), and biotite (2–5 vol. %; 0.2–1.0 mm long), with trace pyroxene (<1 vol. %; 0.5–1.5 mm long) and quartz (<1 vol. %; 0.2–0.5 mm long). Although the

amphibole phenocrysts are euhedral, they are altered, patchy and fractured, and exhibit resorption textures in their cores and rims (Fig. 5f–g). Some amphibole and biotite crystals have rims comprising Fe–Ti oxides. In many samples, plagioclase exhibits patchy and sieve textures.

The granodiorite porphyry is composed of plagioclase, quartz, amphibole, and biotite phenocrysts (30–35 vol. %; 0.3–1.5 mm long) in a congruent groundmass. Most amphibole crystals are euhedral to subhedral, but have been dehydrated (Fig. 5h). Compared to amphibole, biotite and plagioclase are well preserved; the former can contain rare inclusions of zircon and apatite.

Analytical methods

Electron microprobe analysis

The chemical composition of 77 euhedral amphibole grains (one spot on each grain) from pyroxene diorite, granodiorite, and diorite porphyry were determined using a JEOL-8100 electron microprobe (EPMA) at the Electron Probe Laboratory of Northeast Asia, Ministry of Land and Resources of China (MLR), Changchun, China. Backscattered electron images of all amphibole grains show no core to rim or compositional zonation. Measurements were performed on the rims of amphibole grains using a voltage of 20 kv and a current of 1×10^{-8} A. The analysis time was 10 s and the results were corrected using the ZAF algorithm. The following mineral standards from the American National Standard Mineral Bureau were used for instrument calibration — rutile for Ti, diopside for Si, Mg and Ca, orthoclase for K, albite for Na and Al, almandine for Fe, and crocoite for Cr. The chemical compositions of amphibole are presented in Table A.1.

Apatite fission-track analysis

Apatite was separated from three samples of andesite, granodiorite, and granodiorite porphyry collected from the surface outcrops at Naozhi (Fig. 2). Apatite fission-track (AFT) analyses were performed at the Beijing Quick-Thermo Science & Technology Co. Detailed analytical methods are described in Appendix 1.

Apatite and zircon (U-Th)/He dating

Zircon and apatite were separated from two samples of granodiorite and granodiorite porphyry collected from the surface outcrops at Naozhi. All zircon and apatite (U-Th)/He dating was carried out at the University of Melbourne. The analytical procedures followed Gleadow et al (2015), except that for zircons He dating ^{233}U and ^{229}Th spikes were used, and are summarized in Appendix 1.

Results

EPMA major element analyses of amphiboles

All of the analyzed amphiboles are calcic to sodic-calcic (after Leake et al. 1997), containing Ca and Na, in atoms per formula unit (a.p.f.u.), of 1.70–1.89 ($n=77$) and 0.26–0.62 ($n=77$), respectively. The amphiboles from the pyroxene diorite and granodiorite are Mg-hornblende in composition, whereas those from the diorite porphyry are Mg-hornblende to tschermakite in composition (Fig. 6a). This variation in composition is consistent with the broad range of Al in the amphiboles (Fig. 6b).

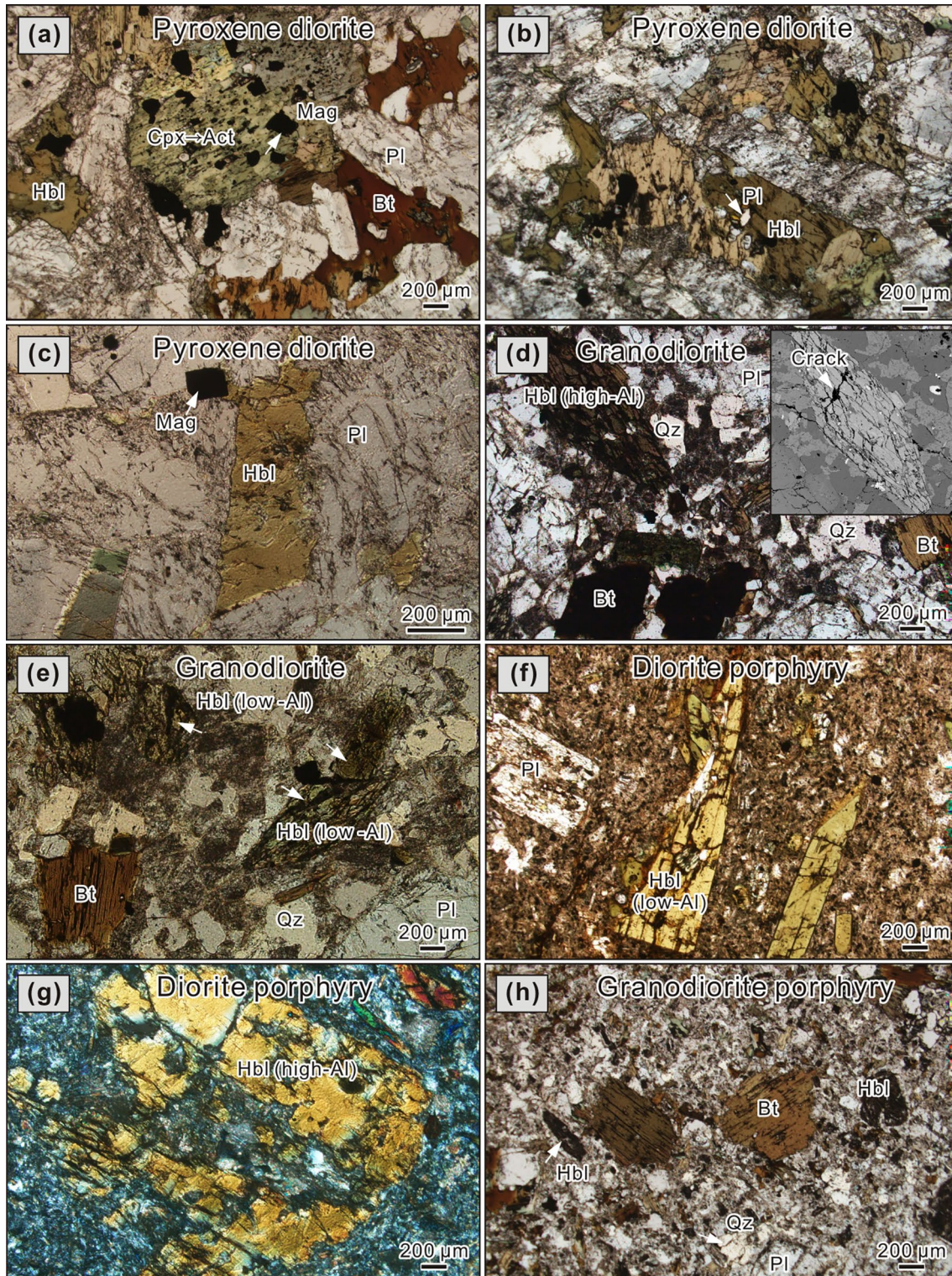
The hornblendes ($n=6$) from two pyroxene diorite samples show a narrow variation in SiO_2 (49.15–49.90 wt. %), FeO (11.42–11.66 wt. %), MgO (14.38–14.88 wt. %), Al_2O_3 (6.06–6.43 wt. %), and CaO (11.62–11.88 wt. %). Compared to the hornblendes from the pyroxene diorite, those ($n=30$) from six granodiorite samples have a greater variation in SiO_2 (44.01–50.56 wt. %), FeO (10.86–14.15 wt. %), MgO (11.46–16.00 wt. %), Al_2O_3 (4.20–10.16 wt. %), and CaO (10.77–11.87 wt. %). The amphiboles ($n=41$) from four diorite porphyry samples contain SiO_2 of 42.69–49.26 wt. %, FeO of 10.38–14.10 wt. %, MgO of 12.07–15.14 wt. %, and Al_2O_3 of 5.35–11.25 wt. %, and CaO of 10.93–11.94 wt. %.

Apatite fission track

Detailed results for three samples are summarized in Table 1. Central AFT ages range from 118.6 ± 3.2 Ma to 121.8 ± 3.7 Ma. The confined mean track lengths (MTLs) vary from 12.8 ± 0.7 μm to 13.2 ± 0.9 μm , with standard deviations (SD) of 1.4–1.5 μm . Dpar values are mostly high, ranging from 1.03 μm to 1.66 μm . Such relatively short MTLs with weak to moderate bimodal distributions (see Figs. 8 below) suggest that these samples have spent considerable time within the AFT partial annealing zone (~60–120 °C; the zone in which the track lengths and fission track ages decrease; Gallagher et al. 1998), as evidenced by younger ages compared to the emplacement ages of their host rocks (129 ± 1 to 126 ± 1 Ma).

Zircon and apatite (U-Th)/He

(U-Th)/He analyses of both zircon and apatite were carried out on two samples with results presented in Tables 2 and 3. Single grain ZHe ages of granodiorite and granodiorite porphyry samples range from 129.4 to 87.8 Ma and from 240.7 to 123.6 Ma, respectively. Such overdispersed ages exceed the analytical uncertainty. Several factors, such as the



existence of U- and/or Th-rich mineral inclusions, heterogeneous distribution of parent nuclides, difference in grain size, and radiation damage caused by radioactive decay, could lead to these overestimated or underestimated ages (e.g., Reiners 2005; Danišik et al. 2017; Morón et al. 2020

and references therein). Two relatively young ZHe ages of 87.8 ± 0.9 Ma and 116.1 ± 7.1 Ma relative to the AFT ages of ~ 120 Ma (Fig. 7a), can be attributed to their relatively high eU (> 1000 ppm), resulting from He diffusion related to radiation damage (e.g., Guenther et al. 2013). Several

Fig. 5 Photomicrographs of dioritic to granitic phases of the intrusive complex. **a** Complete replacement of clinopyroxene by actinolite, with magnetite inclusions. Biotite, with small plagioclase inclusions, and amphibole are interstitial to plagioclase grains, suggesting a later crystallization or subsolidus origin. **b** Hornblende cumulates are interstitial to plagioclase grains. **c** Euhedral hornblende lacking an opacite rim coexisting with tabular plagioclase grains, indicative of equilibrium with host melts. **d** Fractured euhedral hornblende (BSE photo at top right) without a reaction texture surrounded by subhedral plagioclase and quartz in a granodiorite sample. Subhedral plagioclase and quartz grains enclose euhedral biotite without any reaction textures. **e** Euhedral hornblende and biotite grains surrounded by subhedral plagioclase and quartz grains in a granodiorite sample. **f** Fractured and brecciated hornblende and patchy plagioclase phenocrysts in a diorite porphyry. **g** Resorbed and embayed high-Al amphibole in a diorite porphyry. **h** Completely resorbed hornblende and euhedral biotite phenocrysts in a groundmass of fine quartz and feldspar in a granodiorite porphyry. *Act* actinolite, *Bt* biotite, *Cpx* clinopyroxene, *Hbl* hornblende, *Mag* magnetite, *Pl* plagioclase, *Qz* quartz. Only photomicrograph (**g**) was taken in cross-polarized transmitted light

zircon grains from granodiorite porphyry yielded ZHe ages from 240.7 Ma to 169.2 Ma older than zircon U–Pb ages of ~130 Ma. These overestimated ZHe ages can possibly be attributed to the heterogeneous distribution of U in zircon or the presence of small He-rich fluid inclusions (Danišik et al. 2017) (Fig. 7a). A good positive trend is seen between grain radius and ZHe ages (Fig. 7b), and therefore, the difference in grain size provided certain contributions to ZHe age variation. Collectively, when those outliers are excluded, the remaining ZHe ages are clustered from 123.6 ± 7.7 to 129.4 ± 8.0 Ma, consistent with their U–Pb ages within analytical uncertainties. The apatite grains analyzed from granodiorite and granodiorite porphyry show some AHe age dispersion and range from 91.4 ± 5.7 to 63.1 ± 3.9 Ma and from 62.2 ± 3.9 to 41.0 ± 2.5 Ma, respectively.

Inverse thermal history modeling

To reconstruct the post-mineralization time–temperature history of the Naozhi system, thermal history modelling was performed on AFT data using the HeFTy v.1.9.3 software (Ketchum et al. 2007). A modelled path that matches the input data with a goodness of fit of > 0.05 is considered “acceptable”, and if the goodness of fit is > 0.5 , the modelled path is considered “good”. Based on the observation that the andesite of 130 ± 2 Ma is overlain by the younger volcanic sediments of 108 ± 2 Ma, we highlighted the andesite was exposed but the intrusive complex probably was still concealed at this time. Considering latter has the AFT ages comparable with exposed andesite, they must have experienced a similar heating process at about 108 ± 2 Ma when the > 1 km thick covering occurred. The evaluated preservation temperatures of 40 to 80 °C are considered as a time–temperature constraint. AHe and ZHe ages with their He partial retention zones were set as low-temperature constraints of 35 to 80 °C

(Farley and Stockli 2002) and high-temperature constraints of 130 to 200 °C (Wolfe and Stockli 2010), respectively. We did not attempt to model AFT sample NZ12 of andesite due to few age grains and track lengths being available for measurement. Using a present-day surface temperature of 10 ± 10 °C, the inverse modelling software was run until 100 good paths were obtained; with results shown in Fig. 8. The predicted results from the best-fit paths are consistent with those obtained results. The models indicate two phases of cooling and one phase of heating—a rapid cooling phase following emplacement of the intrusive rock at ca. 130 Ma, moderate heating from 130 to 106 Ma, and slow cooling from 106 Ma to the present day.

Discussion

Evolution of the intrusive complex

The igneous mafic microgranular enclaves (MMEs; 55.7–56.0 wt. % SiO_2 ; Fig. 9a) found in the granodiorite phase (62.3–66.9 wt. % SiO_2), together with disequilibrium plagioclase textures (found only where the MMEs occur) with felsic cores and relatively mafic rims enclosing microcrystalline amphibole and acicular apatite (Fig. 9b), indicate rapid cooling of mafic melts that intruded relatively cold felsic melts (Liu et al. 2020). The repeated recharge of mafic melts into porphyry systems has been proposed as a source of metals and sulfur (e.g., Hattori and Keith 2001; Halter et al. 2005; Audétat and Pettke 2006; Sillitoe 2010; Hollings et al. 2013; Cao et al. 2018). Although this magma mingling could have potentially affected the compositions of minerals in the crystallizing magmas (e.g., Foley et al. 2013), the lack of compositional zonation of individual amphibole suggests a stable regime where the minerals are in constant equilibrium with the host melts. In addition, there is only rare evidence for mingling throughout the intrusive complex, we propose that there was a process of thorough mixing between the mafic and felsic melts to form a relatively homogeneous magma.

Temperature–pressure conditions: Aluminum-in-amphibole thermobarometry has been widely used to estimate the temperature and pressure conditions under which amphiboles crystallized, using the formulae of Ridolfi and Renzulli (2012). The amphiboles analyzed in this study are tschermakite to Mg-hornblende in composition. The crystallization temperatures calculated using the Si contents of the amphiboles are 716–938 °C (± 23.5 °C) and correlate positively with pressure ($R^2 = 0.96$; Fig. 10a and b). Estimated pressures of crystallization vary from 0.56 ± 0.06 to 3.25 ± 0.37 kbar (Fig. 10a).

Since amphibole compositions are sensitive to temperature, pressure, and liquid composition, Si-in-amphibole

Table 1 Apatite fission-track data of Early Cretaceous andesite (NZ12), granodiorite (NZ118), and granodiorite porphyry (NZ10) at Naozhi

Sample number	Elevation (m)	No. of grains	N _s	ρ _s (10 ⁵ × cm ⁻²)	²³⁸ U (ppm)	Disper- sion (%)	Pooled age (Ma ± 1σ)	Central age (Ma ± 1σ)	NL	MTL (μm ± SE)	SD (μm)	Dpar (μm)	GPS	
													X	Y
NZ12	270	33	672	5.67	9.70	0	117.0 ± 5.4	119.9 ± 4.7	13	12.8 ± 0.7	1.4	1.60	129°40'13"	43°10'02"
NZ118	540	29	1550	9.71	15.89	9	120.4 ± 3.7	121.8 ± 3.7	101	13.2 ± 0.9	1.5	1.03	129°37'11"	43°09'44"
NZ10	350	31	2366	9.07	15.41	8	117.7 ± 3.2	118.6 ± 3.2	102	12.9 ± 1.0	1.4	1.66	129°37'30"	43°10'45"

N_s number of spontaneous tracks counted, ρ_s spontaneous track density, ²³⁸U average uranium concentration, NL number of confined track lengths (TINs) measured, MTL mean confined track length, SE standard error, SD Standard deviation of the track length distribution, Dpar long axis of track etch pit

thermometry and the Al-in-amphibole barometer (Putirka 2016) are utilized here to assess the quality of results from Al-in-amphibole thermobarometry. Pressure–temperature estimates using equations from Putirka (2016) show a relatively broad pressure range of 0.77–4.88 kbar but narrow temperature range of 737–917 °C (Fig. 10b). It is noted that at pressures lower than 1.0 kbar, the pressure estimates are ≤ 0.15 kbar higher than those calculated using the Al-in-amphibole thermobarometer, whereas discrepancies in pressure estimates of 0.38–1.77 kbar can be observed at pressures greater than 1 kbar. The pressures calculated for hornblendes from granodiorite using equations from Anderson and Smith (1995) have a range of 0.57 to 2.05 kbar, similar to those calculated using amphibole–only thermobarometry (Ridolfi and Renzulli 2012). We also noted that both methods provide a similar average pressure of 1.20 ± 0.49 kbar and 1.39 ± 0.55 kbar, respectively (Fig. 11), whereas the pressure calculated using equations from Putirka (2016) is slightly overestimated. Collectively, utilizing Al-in-amphibole thermobarometry of Ridolfi and Renzulli (2012) here provides reasonable constraints on the relatively low pressure–temperature conditions.

The mineral–melt Fe/Mg exchange coefficient ($K_D(\text{Fe-Mg})^{\text{mineral-melt}}$) is considered as the criterion of whether equilibrium was achieved between amphiboles and coexisting melts (Putirka 2008, 2016). The $K_D(\text{Fe-Mg})^{\text{Amp-melt}}$ values of 0.28 ± 0.11 are considered to represent the amphibole–melt equilibrium (Putirka 2016). The $K_D(\text{Fe-Mg})^{\text{Amp-melt}}$ values for the three intrusive rocks range from 0.34 to 0.67 (melt compositions from Liu et al (2021); Fig. 12). Only 5% of the 77 $K_D(\text{Fe-Mg})^{\text{Amp-melt}}$ values from these rocks are in equilibrium. All hornblendes from the pyroxene diorite are in nonequilibrium with their host melts, with a narrow range of $K_D(\text{Fe-Mg})^{\text{Amp-melt}}$ values ranging from 0.49 to 0.51, as evidenced by their resorbed texture. Only 10% of the 30 $K_D(\text{Fe-Mg})^{\text{Amp-melt}}$ values from granodiorite are in equilibrium. Based on $K_D(\text{Fe-Mg})^{\text{Amp-melt}}$ values of 0.39–0.67 obtained, only one out of 41 amphiboles from the diorite porphyry is in equilibrium with the host melt (Fig. 12).

The relatively low pressure values of 0.56 to 0.57 kbar which characterize those unfractured, tetragonal and rhombic hornblendes, suggest that they are in equilibrium with granodiorite melts at Naozhi. This is consistent with the minimum pressure estimate of 0.49 kbar at which hornblende can crystallize from a granitic melt (Sato et al. 1999). These hornblendes lie above the actinolite stability field, but below the solidus for tonalite (Anderson et al. 2008; Lledo and Jenkins 2008) (Fig. 10), indicative of a low-pressure setting and a high-level intrusion of ≤ 2.1 km depth (based on a specific weight of continental crust of 2.7 g/cm³). The relatively high pressures of the remaining amphiboles from the intrusive ranging from 0.72 to 3.25 kbar are equivalent to

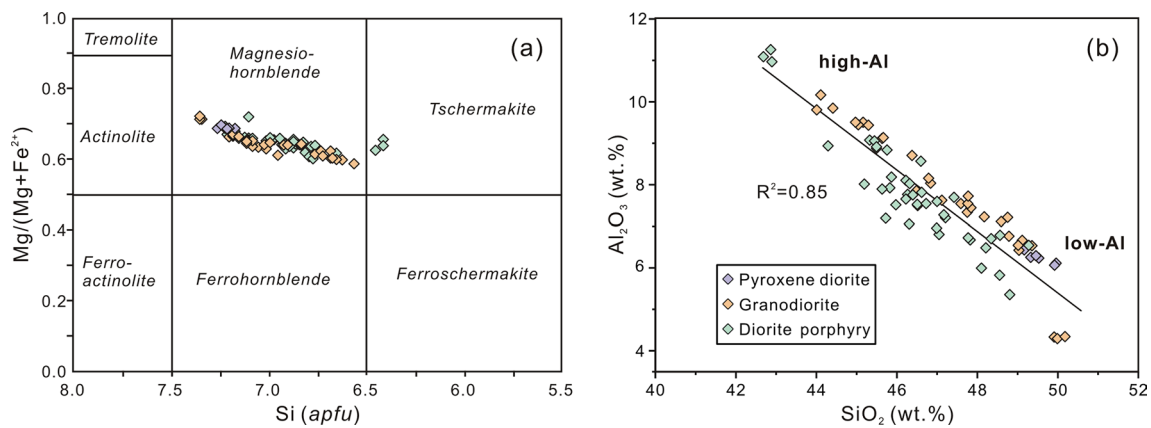


Fig. 6 **a** Mg/Mg + Fe vs. Si (a.p.f.u) amphibole classification diagram (after Leake et al. 1997). The amphiboles from the intrusive complex are tschermakite to Mg-hornblende. **b** SiO₂ vs. Al₂O₃ content of amphibole. Note the clear negative relationship between Al₂O₃ and SiO₂

depths of ~2.7–12.0 km and temperatures of ~767–938 °C. Collectively, the crystallization pressures of these amphiboles span those typical of mid- to upper-crustal levels, where the parental magmas evolved towards higher silica content. It is noted that such a wide range of pressures only characterize amphiboles in the diorite porphyry with intermediate emplacement, but when considered together with resorption textures and dehydration of amphibole in porphyritic intrusions, different magma sources are implied, with relatively high-pressure amphibole being sourced from deep magmas. The presence of igneous MMEs and disequilibrium textures of plagioclase implies magma mixing (Fig. 9). We attribute this mixing to recharge of the system by rapidly ascending mafic magmas, which could have transported deeper sourced amphibole crystals to shallower levels.

Oxygen fugacity: The Mg* (magnesium index) of amphibole was used to constrain the oxygen fugacity of the magmas using the relationship $\Delta\text{NNO} = 1.644 \text{ Mg}^* - 4.01$ (Ridolfi et al. 2010) (NNO is the nickel–nickel–oxide buffer). Calculated oxygen fugacities ($f\text{O}_2$) show a broad range from log $f\text{O}_2$ of –13.30 to –10.70, with errors of 0.4 at 0.56–3.25 kbar, but generally correlate positively with pressure (Fig. 13a). The low pressure (< 1 kbar) amphiboles record more oxidized conditions, with ΔNNO of 1.01 to 2.07 (mean = 1.43 ± 0.26 ; 1SD; $n = 18$), than the relatively higher pressure (1–4 kbar) amphiboles, with ΔNNO –0.10–1.54 (mean = 0.75 ± 0.36 ; 1SD; $n = 59$). The presence of magmatic magnetite at Naozhi is consistent with a relatively oxidized magma.

H₂O content: The ^{VI}Al* (octahedral aluminium index) value of amphibole was used to estimate the water content of the magmas using the relationship $\text{H}_2\text{O}_{\text{melt}} = (5.215 \times \text{VIAl}^*) + 12.28$ (Ridolfi et al. 2010). Collectively, the magmas parental to the intrusive complex of the Naozhi system are hydrous and generally contain > 4 wt. %H₂O (Fig. 13b). The broad range of calculated water

content between 2.25–6.57 wt. % could be explained by the dependance of H₂O solubility on pressure (Holtz et al. 1995).

Interpretations of the thermochronological data

Previous geochronologic studies on the mineralized igneous rocks and hydrothermal minerals at Naozhi yielded Early Cretaceous ages of 130 ± 2 Ma for the andesites, 129 ± 1 to 126 ± 1 Ma for the intrusive complex (zircon U–Pb dating), and an Ar–Ar plateau age of 129 ± 1 Ma for hydrothermal sericite. Since the ZHe ages of granodiorite and granodiorite porphyry are comparable with their zircon U–Pb ages, a rapid cooling of intrusive rocks through 200 °C and even below 130 °C probably occurred.

Considering that most epithermal deposits form at depths of < 1 km, there must have been several hundred meters of erosion from the epithermal sector of the Naozhi system. In an ideal geologic environment, with rapidly cooled volcanic or very high-level intrusive rocks that have not been buried to > 1 km depth, AFT ages would be expected to yield a reliable measure of the age of formation of the host rock (Gleadow et al. 1986). Although all apatite samples in this study yield similar central FT ages at the 2 σ level, the AFT ages of 122–119 Ma are about 10 m.y. younger than the zircon U–Pb ages of 129–127 Ma for the host rocks. This could be the result of an increase in the ambient temperature in excess of ~60 °C after formation, caused either by burial or by some other heating mechanism (Gleadow et al. 1986). As shown in Fig. 8, the highest post-mineralization temperatures were attained at ~106–110 Ma, synchronous with deposition of the post-mineralization pyroclastic cover (108 ± 2 Ma). This volcanism could possibly have resulted in a pronounced change in ambient temperature. It is important to note that the slightly shorter mean confined track lengths of apatite samples in this study compared to those

Table 2 Single grain zircon (U-Th)/He data

Rock type	Sample	⁴ He (ncc)	Mass (ug)	F _T ^a	U (ppm)	Th (ppm)	Th/U ratio	[eU] ^b (ppm)	Corrected age (Ma)	Error (±1σ)	Grain length (um)	Grain half width (um)	Rs ^c	Crystal morphology ^d
Granodiorite	D3083	10.42	2.7	0.74	209.3	141.6	0.68	242.6	129.4	8.0	155.5	47.3	54.4	2 T
		14.28	5.7	0.80	111.0	55.9	0.50	124.1	162.8	10.1	220.6	53.7	64.8	2 T
		20.26	1.1	0.67	1658.5	419.6	0.25	1757.1	87.8	5.4	109.2	37.6	41.9	2 T
		18.93	1.8	0.71	605.9	339.0	0.56	685.6	127.1	7.9	129.8	43.8	49.2	2 T
Granodiorite Porphyry	D4114	33.036	1.1	0.66	1723.6	1490.6	0.86	2073.8	116.1	7.2	104.8	46.2	48.1	2 T
		46.10	6.0	0.79	330.5	163.0	0.49	368.8	169.2	10.5	259.4	47.5	60.3	2 T
		51.70	5.7	0.80	272.7	149.1	0.55	307.7	237.3	14.7	230.2	51.3	62.9	2 T
		37.71	4.0	0.76	363.2	233.4	0.64	418.1	181.5	11.3	219.3	42.9	53.8	2 T
		40.83	5.7	0.79	215.9	103.6	0.48	240.2	240.7	14.9	250.9	47.3	59.7	2 T
		40.65	5.2	0.78	239.2	157.8	0.66	276.3	226.9	14.1	239.4	46.8	58.7	2 T
		32.906	3.7	0.76	510.8	292.9	0.57	579.6	123.6	7.7	210.5	42.5	53.0	2 T
		40.686	4.0	0.76	524.1	383.4	0.73	614.2	134.7	8.4	205.5	45.4	55.7	2 T

^aF_T is the α-ejection correction after Farley et al. (1996)

^bEffective uranium concentration (U ppm + 0.235 Th ppm)

^cEquivalent spherical radius (Rs) = (3*R*L)/(2*(R+L)) after Beucher et al. (2013)

^dGrain morphology: 0 T=no terminations, 1 T=one termination, 2 T=2 terminations

Table 3 Single grain apatite (U-Th)/He data

Rock type	Sample	⁴ He (ncc)	Mass (ug)	F ₇ ^a	U (ppm)	Th (ppm)	Sm (ppm)	Th/U ratio	[eU] ^b (ppm)	Uncor- rected age (Ma)	Corrected age (Ma)	Error (± 1σ)	Grain length (um)	Grain half width (um)	Crystal morphology ^c
Granodiorite	NZ118	0.798	0.00442	0.72	14.20	53.8	150.7	3.79	26.8	54.7	75.6	4.7	248.9	49.6	1 T
		4.180	0.02528	0.84	9.10	38.6	115.7	4.23	18.2	73.7	87.3	5.4	320.4	88.6	0 T
		3.055	0.02802	0.84	6.90	27.2	82.2	3.95	13.3	66.5	79.3	4.9	454.1	78.3	0 T
		0.437	0.00495	0.72	7.50	35.5	105.8	4.73	15.8	45.3	63.1	3.9	236.5	45.6	0 T
Granodiorite Por- phyry	NZ-10	1.997	0.00961	0.77	11.30	54.5	111.3	4.83	24.1	70.1	91.4	5.7	273.8	65.0	2 T
		0.476	0.00642	0.73	9.50	44.7	163.9	4.70	20.0	30.1	41.0	2.5	242.1	56.5	2 T
		0.450	0.00430	0.69	12.80	62.9	182.0	4.90	27.6	30.8	44.6	2.8	223.4	48.1	2 T
		1.123	0.00916	0.77	11.00	47.7	172.9	4.32	22.2	44.7	58.2	3.6	248.5	66.6	2 T
		1.031	0.00821	0.76	10.70	45.9	159.8	4.30	21.5	47.4	3.9	231.5	65.3	2 T	
		0.685	0.00603	0.72	12.50	54.3	176.4	4.33	25.3	36.5	50.3	3.1	252.4	53.6	2 T

^aF₇ is the α-ejection correction after Farley et al. (1996)^bEffective uranium concentration (U ppm + 0.235 Th ppm)^cGrain morphology: 0 T = no terminations, 1 T = one termination, 2 T = 2 terminations

from undisturbed igneous rocks (13–16 μm) (Gleadow et al. 1986) (see Table 1 and Fig. 8), suggest that they experienced partial thermal resetting in the AFT partial annealing zone (~60–120 °C; Wagner and Haute 1992). We attribute this thermal resetting to volcanic activity at this time and because their AFT systems were only partially reset, the calculated ages taken at face value do not in themselves directly date a discrete geological event.

The inverse thermal history modelling results indicate rapid cooling following emplacement of the parent magma itself. The igneous rocks were preserved at temperatures of < 60 °C at ca. 130 Ma, suggesting a high-level emplacement at crustal levels of < 2 km. Such shallow emplacement is supported by the fluid mineralization at a maximum 169 bar of pressure, corresponding to a ~1.7 km depth assuming a hydrostatic load (Liu et al. 2022). The following period of heating to temperatures > ~60° but < ~85 °C (Fig. 8) is here attributed to burial by a kilometer or more of the dacitic pyroclastic suite of 108 ± 2 Ma. This scenario is consistent with a preservation thickness of 1.6 km of the regional ~108 Ma volcanics (Shi 2008). Accordingly, we propose that burial by the young dacitic pyroclastic suite is responsible for the increase in temperature of the underlying, pre- and syn-mineralization intrusive complex at 110–106 Ma (Fig. 8). The post-mineralization burial protected the hydrothermal ores from extensive erosion, which may explain why the Naozhi deposit is the only ~130 Ma deposit preserved in the area, whereas most other hydrothermal Cu–Au deposits are 100–110 Ma in age (Ren et al. 2016). In addition, it is noted that AHe ages (which are considered as transient points on a cooling curve) for granodiorite porphyry are younger than those of granodiorite, which records early cooling for the latter through the He partial retention zone of ~35 to 80 °C. This differential cooling may be related to the sample elevation gaps of about 200 m, with granodiorite sampled from higher levels (Table 1). The much uplifting of granodiorite stock probably is related to the young but unknown structural events that likely steeply tilted the volcanic layers at Naozhi. Verifying the structural events is beyond the scopes of this paper. As shown in Fig. 8, a period of protracted slow cooling post-dated burial by a post-mineralization volcanic section, which is likely due to erosion of this cover and some ~130 Ma material.

Implications for the porphyry Cu system

Nature of the host magmas: Most porphyry Cu deposits are associated with oxidized, sulfur-rich, and hydrous arc-related magmas. Several studies have demonstrated that fertile magmas are characterized by a higher oxidation state than barren magmas (Ballard et al. 2002; Burnham et al. 2015; Dilles et al. 2015; Lu et al. 2016). Although exceptionally high melt *f*O₂ may not be fundamental to the formation

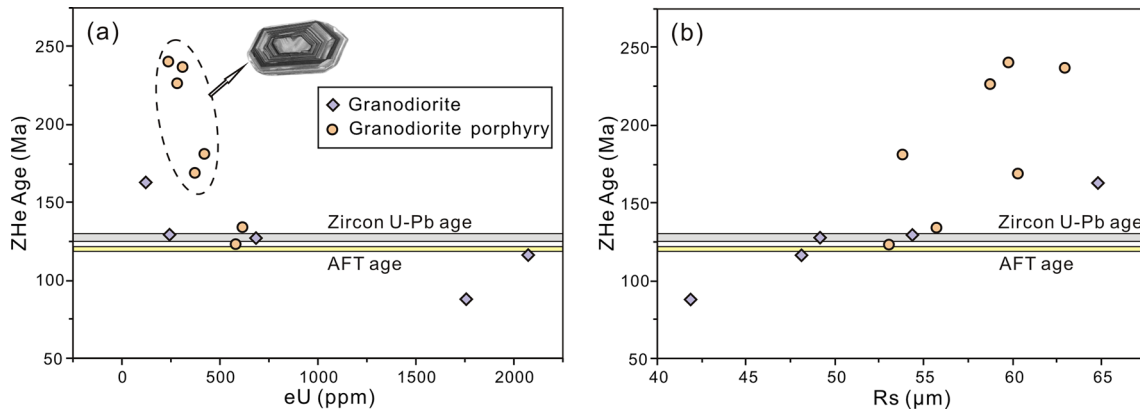
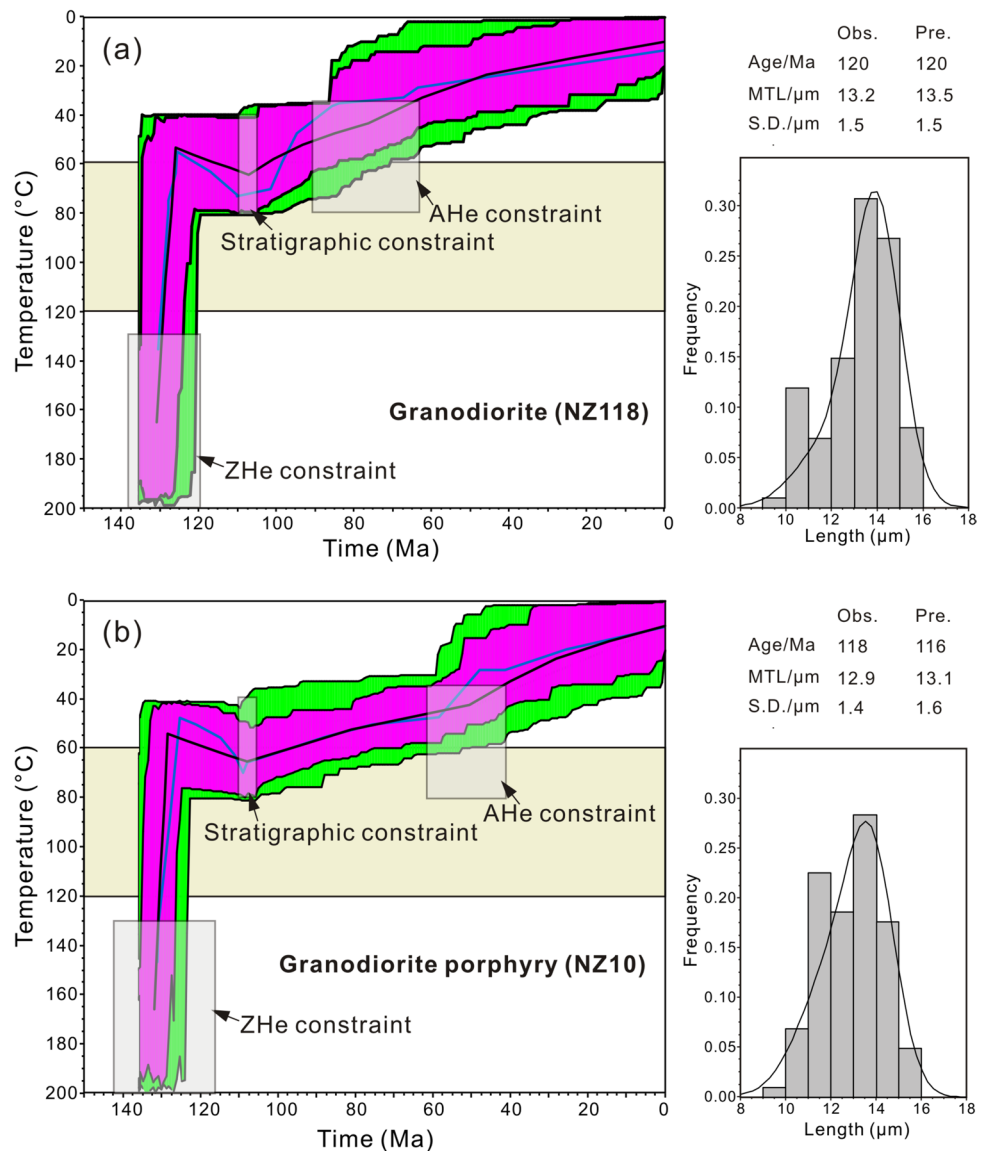


Fig. 7 Correlations of **a** U with zircon (U–Th)/He ages and **b** grain radius (Rs) with zircon (U–Th)/He age

Fig. 8 Modeled time–temperature paths (left) and confined track length distribution (right) for apatite analyzed from granodiorite and granodiorite porphyry at Naozhi. Modeling was conducted using the HeFTy software of Ketcham et al (2007). The models are based on AFT data with ZHe and AHe ages and stratigraphic records used as constraints, together with a present-day surface temperature of $\sim 10 \pm 10$ °C. The green envelopes denote all of the acceptable time–temperature paths, with a goodness of fit > 0.05 , whereas the purple envelopes represent all of the good time–temperature paths, with a goodness of fit > 0.5 . The thick blue and black line represents the best-fit modelling and weighted mean cooling path for each plot, respectively. The pale-yellow areas denote the apatite partial annealing zone (APAZ; 60–120 °C; Gallagher et al. 1998). *Obs.* obtained results, *Pre.* predicted results, *MTL* mean confined track length, *SD* standard deviation



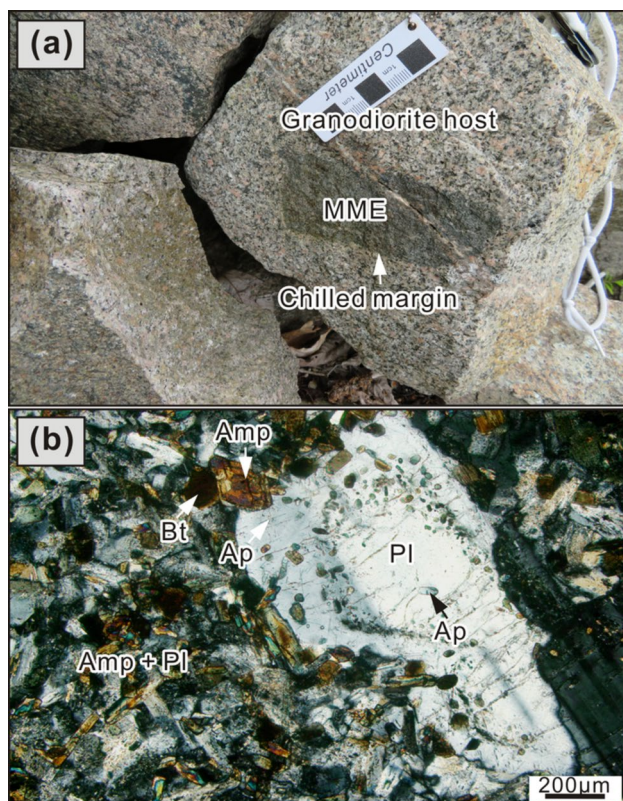


Fig. 9 Examples of magma mixing textures. **a** Mafic microgranular enclave (MME) in a granodiorite host rock, with chilled margins. **b** Photomicrograph of a MME mainly composed of fine-grained amphibole, plagioclase, and biotite. The plagioclase phenocryst comprises two continuously zoned generations—an early Na-rich core that contains low-temperature, columnar apatite, and a late Ca-rich rim enclosing abundant amphibole and biotite microcrystals and acicular apatite. *Amp* amphibole, *Ap* apatite, *Bt* biotite, *Pl* plagioclase

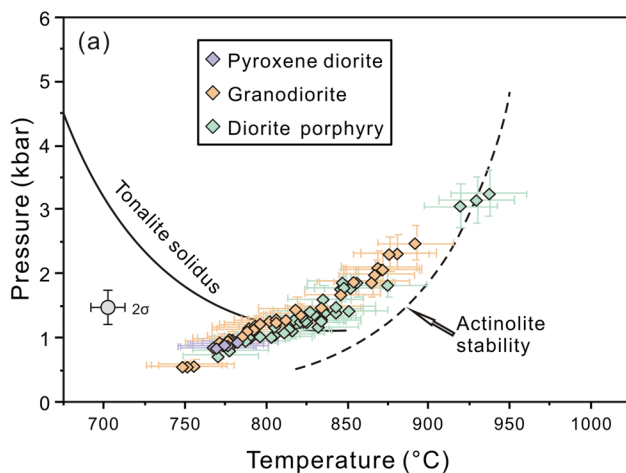
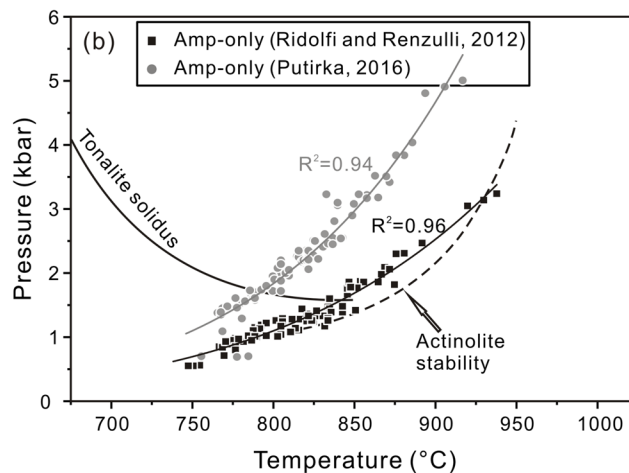


Fig. 10 Calculated crystallization conditions of amphibole from the Naozhi intrusive complex. **a** The amphiboles crystallized from magmas at pressures of <1 to 4 kbars at temperatures of 700 °C to <1000 °C, with a high level of equigranular pyroxene diorite and granodiorite, based on the Al-amphibole-only thermobarometer

of porphyry Cu deposits (Matjuschkin et al. 2016; Du and Audétat 2020), oxidized conditions are conducive to the effective transport of metals and sulfur as they can occur in multiple valence states (Richards 2011a). For this reason, the chalcophile metals would be dissolved more readily by hydrothermal fluids that exsolve from shallow, volatile-saturated magma reservoirs. There is a general consensus that the causative magmas in porphyry systems are derived from depths of 5–15 km (e.g., Sillitoe 2010). There is a positive correlation between the oxygen fugacity and pressure of the magmas, and the shallow intrusive stocks had a dramatic drop in fO_2 relative to those source magmas at > 1.5 kbar in the Naozhi system (Fig. 13a). We interpret the decrease of fO_2 with decreasing pressures to reflect decompression and devolatilization (crystallization-driven second boiling) of the ascending magmas (Candela 1986). There is an inverse correlation of NNO values with pressure for Naozhi, with the shallow melts being more oxidized (Fig. 13a). Similar changes in oxidization state as the magma with evolution have been recognized by Ballard et al (2002) and Cocker et al (2016) using the zircon oxybarometer. This self-oxidization process is due to the loss of H_2 to the segregating fluid during molecular dissociation of H_2O ; an alternative scenario responsible for the oxidizing process is the partitioning of oxidized sulfur from the melt into the hydrothermal fluid both oxidise iron in the residual melt (Loucks et al. 2018 and references therein).

High water content in arc magmas is a prerequisite to the formation of porphyry systems (Richards 2011b), as hydrous (> 5 wt. % H_2O) magmas can exsolve sufficient metalliferous fluid to generate large magmatic–hydrothermal ore systems (Chiaradia and Carrichi 2017). The parental magmas



(Ridolfi and Renzulli 2012). **b** A comparison of pressure estimates calculated using different thermobarometers from Ridolfi and Renzulli (2012) and Putirka (2016). The tonalite solidus curve is from Anderson et al (2008) and the Fe-actinolite stability curve is from Lledo and Jenkins (2008). *Amp* amphibole

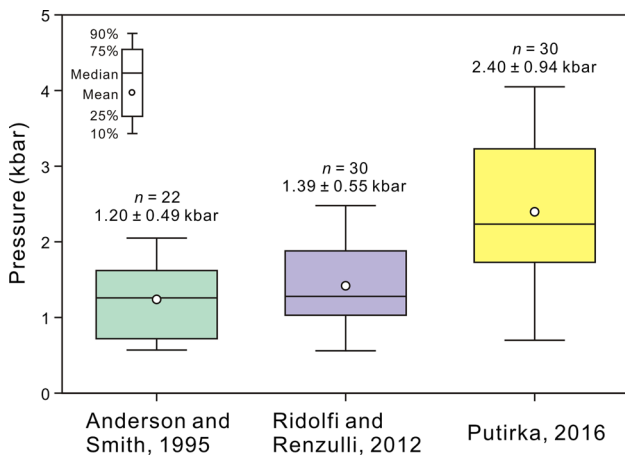


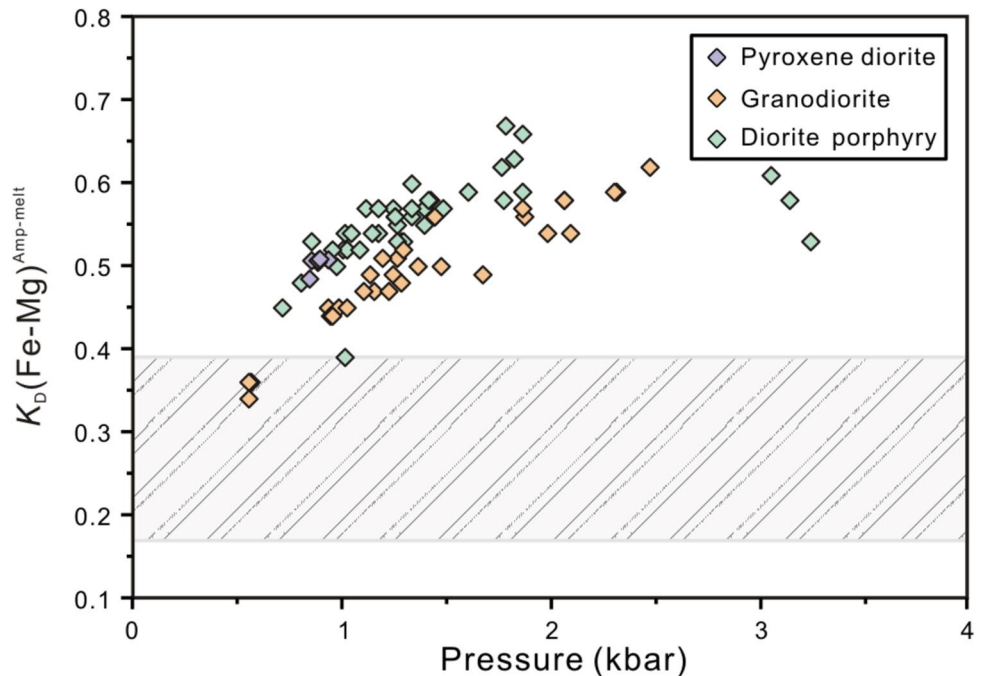
Fig. 11 Box diagram illustrating the pressure estimates for hornblendes from the granodiorite using different thermobarometers from Anderson and Smith (1995), Ridolfi and Renzulli (2012), and Putirka (2016)

at Naozhi have variable H₂O contents, ranging from 7.57 to 2.25 wt. %. The water content of these magmas is higher than the H₂O solubility of dacitic (Moore et al. 1998) and andesitic melts (Botcharnikov et al. 2015) only at pressures of <2.5 kbar (Fig. 13b), suggesting that they were water-saturated. The transition to volatile saturation would have driven the exsolution of metal- and S-bearing fluids from the upper layers of the magma reservoir (at depths of 5–15 km) to the shallow hydrothermal mineralizing system, which, together with magma degassing, likely caused the pronounced fluctuations of magmatic water contents from 6.07

to 2.25 wt. % at <2.5 kbar pressures (Fig. 13b). The presence of primary amphibole in the Naozhi intrusive complex is consistent with them having crystallized from hydrous parental magmas, which would delay plagioclase crystallization and result in high Sr/Y values (Richards 2011b). Amphibole fractionation can lead to weak positive Eu anomalies that increase with fractional crystallization (Hao et al. 2017), as exemplified by the El Abra–Pajonal igneous complex in northern Chile (Cocker et al. 2016). Therefore, the decreasing Sr/Y values (54 to 27) that correlate with decreasing Eu/Eu* (1.34 to 0.58; Liu et al. 2021) during magma evolution in the Naozhi system reflects major plagioclase fractionation over amphibole. This hypothesis is supported by plagioclase fractionation becoming increasingly important during a decrease in pressure, accompanied by loss of water in the upper-crustal levels (Loucks 2014; Cocker et al. 2016). Dominant crystallization dominated by plagioclase perhaps implies a relatively long timescale of magma differentiation within a shallow reservoir but not at deep-crustal levels (15–40 km) at which amphibole is dominant fractionation phase (Alonso-Perez et al. 2009; Ridolfi et al. 2010). This magma cumulates and water-saturation at a shallow level rather than at deep-crustal levels facilitated the Au mineralization in porphyry system (see Chiaradia 2022).

Post-mineralization exhumation of the Naozhi system: Many epithermal Au–Cu deposits, particularly intermediate-sulfidation or high-sulfidation type, occur above or on the margins of PCDs (e.g., Simmons et al. 2005; Sillitoe 2010). In some instances, epithermal- and porphyry-style mineralization occurs within several kilometers of each other, where they have been tilted by

Fig. 12 Calculated pressures vs. $K_D(\text{Fe-Mg})^{\text{Amp-melt}}$ for pyroxene diorite, granodiorite, and diorite porphyry. The grey box highlights the analyses that are in Fe/Mg equilibrium with their bulk-rock compositions. The equilibrium values of 0.28 ± 0.11 from Putirka (2016)



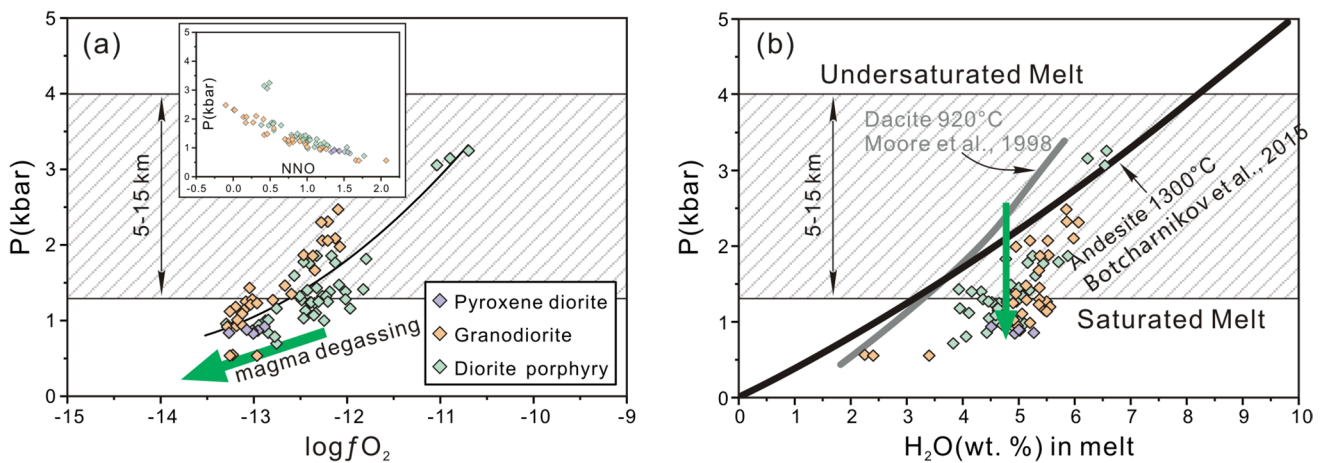


Fig. 13 Oxygen fugacity and water content of the specific magmas that formed the Naozhi intrusive complex. **a** Evolution of oxygen fugacity estimated from amphibole. The rapid drop in $\log f_{\text{O}_2}$ at depths of <5 km is likely the result of magma degassing. Inset (top left) shows the negative correlation between ΔNNO and pressure, with shallow magmas being more oxidized. **b** H_2O content of the magmas continuously decreases with decreasing pressure. A transi-

tion to water saturation of the magmas occurred at pressures of <2.5 kbar. The fluctuation in H_2O content (6.53 to 2.26 wt. %) of shallow magmas (<2.5 kbar) was likely caused by the exsolution of fluids and magma degassing. The thick gray and black lines represent the solubility of H_2O in dacitic melts at 920 °C (Moore et al. 1998) and in andesitic melts at 1300 °C (Botcharnikov et al. 2015), respectively

post-mineralization deformation (Seedorff et al. 2005). As mentioned above, the 130 Ma andesite at Naozhi is only exposed near the epithermal mineralization, supporting a higher degree of exhumation near the porphyry core of the Naozhi magmatic–hydrothermal system. Since the amphiboles analyzed here crystallized at an early stage during magmatic evolution, the Al-in-amphibole thermobarometer yielded a maximum estimate of 2.1 km for the emplacement paleodepths for the present intrusive complex. Based on geological preservation and thermochronology, the paleodepths of the andesite and intrusive complex that hosts the porphyry-style mineralization were constrained to <1 km and <2 km, respectively. The Batu Hijau porphyry Cu–Au deposit in Indonesia is considered a comparable example to the Naozhi system, where the polymetallic veins were overlain by post-mineralization volcanic rocks. The tonalitic magmas at Batu Hijau had a final crystallization and emplacement depth of <2 km (± 0.5 km), based on Al-in-amphibole thermobarometry (Garwin 2000).

Exposing rocks that were emplaced initially at different depths to a similar horizontal level at Naozhi requires varying degrees of erosion and/or uplift. The different degrees of unroofing may be related to the ca. 108 Ma volcanic cover and/or young structural events, but further detailed structural reconstructions would be required to assess this possibility. At least 1 km of post-mineralization cover would have minimize the loss of metals during prolonged erosion that removed <2 km of pre-mineralization material from the top of the Naozhi magmatic–hydrothermal system during the last ~ 130 m.y., suggesting an erosion

rate of ~ 23 m/m.y.r., with a rapid exhumation during 130–110 Ma.

Conclusion

The 130 Ma magmatic–hydrothermal event at Naozhi is genetically associated with porphyry- and epithermal-style mineralization. The magmas that fed the Naozhi porphyry system had high water content (mostly >4 wt. %) and were moderately oxidized ($\Delta\text{NNO} -0.35$ to 2.21), which was conducive to the transportation of metals during magma ascent. Following evolution in the shallow crust, the magmas exsolved a magmatic aqueous phase and released volatiles at <2.5 kbar pressures, which caused a rapid decrease in oxygen fugacity ($\log f_{\text{O}_2} -14.13$ to -10.96) and water content (6.53–2.26 wt. %). Ore formation occurred at paleodepths of <1 km for the peripheral epithermal veins, based on geological preservation, and <2 km for the core of the porphyry, based on thermochronological data and thermal history modelling. Together, these paleodepths are roughly consistent with an emplacement depth of <2.1 km for the intrusive complex, based on amphibole geobarometry. A post-mineralization volcanic cover at ca. 108 Ma protected the ore deposits from extensive erosion, resulting in a high-level of preservation of Naozhi porphyry system.

Appendix

See Table 4

Table 4 Composition of amphibole from the intrusive complex at Naozhi

Intrusive phase	Pyroxene diorite														
SiO ₂	49.15	49.31	49.94	49.51	49.90	49.44									
TiO ₂	1.54	1.54	1.47	1.43	1.46	1.59									
Al ₂ O ₃	6.43	6.25	6.11	6.23	6.06	6.29									
FeO	11.64	11.66	11.53	11.66	11.42	11.59									
MnO	0.17	0.29	0.26	0.26	0.32	0.30									
MgO	14.49	14.59	14.38	14.54	14.88	14.39									
CaO	11.69	11.62	11.88	11.76	11.73	11.72									
Na ₂ O	1.09	1.08	0.95	0.93	0.91	0.91									
K ₂ O	0.77	0.51	0.56	0.61	0.57	0.66									
Total	97.02	96.88	97.09	96.96	97.25	96.89									
Si	7.17	7.20	7.26	7.22	7.24	7.21									
Al ^{IV}	0.83	0.80	0.74	0.78	0.76	0.79									
Al ^{VI}	0.28	0.271	0.31	0.29	0.28	0.30									
Ti	0.17	0.17	0.16	0.17	0.16	0.16									
Fe ³⁺	0.00	0.00	0.00	0.00	0.00	0.00									
Fe ²⁺	1.43	1.43	1.41	1.43	1.40	1.43									
Mn	0.02	0.04	0.03	0.03	0.04	0.04									
Mg	3.15	3.17	3.12	3.16	3.22	3.13									
Ca	1.83	1.82	1.85	1.84	1.82	1.83									
Na	0.31	0.31	0.27	0.26	0.26	0.26									
K	0.14	0.10	0.10	0.11	0.11	0.12									
T (°C) ^a	782	776	767	773	769	774									
P (kbar) ^a	1.02	1.02	0.93	1.02	0.98	0.99									
H ₂ O _{melt} (wt.%)	4.51	5.02	5.27	5.02	4.93	5.00									
logfO ₂	-12.89	-12.96	-13.27	-13.02	-13.01	-13.08									
ΔNNO	1.37	1.43	1.33	1.44	1.55	1.36									
T (°C) ^b	781	778	766	769	768	772									
P (kbar) ^b	1.55	1.47	1.39	1.46	1.36	1.49									
FeO _{melt}	7.62	7.62	7.62	7.62	7.62	7.62									
MgO _{melt}	3.29	3.29	3.29	3.29	3.29	3.29									
K _D (Fe-Mg) ^{Amp-melt}	0.51	0.51	0.51	0.51	0.49	0.51									
Intrusive phase	Granodiorite														
SiO ₂	49.02	49.10	49.34	49.00	47.58	48.16	47.74	47.11	45.63	44.01	44.41	46.48	47.83	45.16	45.04
TiO ₂	1.43	1.53	1.62	1.55	1.66	1.68	1.78	1.92	2.53	2.84	2.76	2.11	1.74	2.64	2.05
Al ₂ O ₃	6.42	6.66	6.53	6.54	7.54	7.22	7.33	7.62	9.11	9.80	9.84	7.85	7.44	9.50	9.44
FeO	12.32	12.34	12.22	12.14	12.86	12.31	12.94	13.11	13.38	13.65	13.60	12.88	12.31	13.86	12.97
MnO	0.41	0.18	0.38	0.35	0.44	0.57	0.24	0.41	0.51	0.21	0.34	0.40	0.32	0.28	0.34
MgO	13.82	13.95	14.04	14.07	12.74	13.33	12.92	12.71	12.13	11.59	11.58	13.07	13.18	12.00	12.19
CaO	11.06	11.17	11.27	11.03	11.18	10.77	10.90	10.87	11.02	11.06	11.04	10.81	10.88	11.31	11.42
Na ₂ O	1.55	1.54	1.51	1.48	1.69	1.71	1.70	1.79	1.97	2.05	2.01	1.80	1.63	2.05	2.08
K ₂ O	0.57	0.48	0.53	0.60	0.67	0.52	0.53	0.61	0.80	0.76	0.76	0.67	0.66	0.94	0.71
Total	96.63	96.95	97.51	96.83	96.41	96.29	96.11	96.19	97.13	96.04	96.44	96.09	96.02	97.75	96.27
Si	7.20	7.18	7.18	7.18	7.05	7.11	7.08	7.01	6.76	6.62	6.65	6.92	7.08	6.68	6.73
Al ^{IV}	0.80	0.82	0.82	0.82	0.95	0.89	0.92	0.99	1.24	1.38	1.35	1.08	0.92	1.32	1.27
Al ^{VI}	0.31	0.33	0.30	0.31	0.37	0.36	0.36	0.34	0.36	0.36	0.38	0.30	0.38	0.33	0.39
Ti	0.16	0.17	0.18	0.17	0.18	0.19	0.20	0.21	0.28	0.32	0.31	0.24	0.19	0.29	0.23
Fe ³⁺	0.29	0.29	0.28	0.33	0.22	0.31	0.27	0.28	0.26	0.23	0.24	0.35	0.27	0.22	0.19
Fe ²⁺	1.23	1.22	1.21	1.16	1.41	1.21	1.35	1.36	1.42	1.51	1.49	1.24	1.27	1.52	1.47
Mn	0.05	0.02	0.05	0.04	0.06	0.07	0.03	0.05	0.06	0.03	0.04	0.05	0.04	0.03	0.04
Mg	3.03	3.04	3.05	3.07	2.82	2.93	2.86	2.82	2.68	2.60	2.58	2.90	2.91	2.65	2.72
Ca	1.74	1.75	1.76	1.73	1.77	1.70	1.73	1.73	1.75	1.78	1.77	1.73	1.73	1.79	1.83
Na	0.44	0.44	0.43	0.42	0.49	0.49	0.49	0.52	0.57	0.60	0.58	0.52	0.47	0.59	0.60
K	0.11	0.09	0.10	0.11	0.13	0.10	0.10	0.11	0.15	0.15	0.15	0.13	0.12	0.18	0.14

Table 4 (continued)

Intrusive phase	Granodiorite															
T (°C) ^a	771	777	777	776	802	789	793	806	854	881	876	821	796	871	869	
P (kbar) ^a	0.94	0.99	0.95	0.96	1.27	1.16	1.20	1.30	1.88	2.32	2.31	1.37	1.23	2.07	2.10	
H ₂ O _{melt} (wt.%)	4.90	5.20	4.98	4.79	5.50	5.46	5.56	5.37	5.53	5.86	6.07	4.95	5.36	5.20	5.98	
logfO ₂	-13.29	-13.18	-13.19	-13.13	-13.09	-13.11	-13.20	-13.02	-12.47	-12.21	-12.28	-12.60	-13.04	-12.27	-12.13	
ΔNNO	1.19	1.19	1.17	1.26	0.72	0.97	0.81	0.70	0.27	0.01	0.02	0.80	0.90	0.14	0.31	
T (°C) ^b	783	787	789	788	805	803	803	815	858	881	876	831	805	870	863	
P (kbar) ^b	1.57	1.67	1.59	1.62	2.21	2.01	2.09	2.27	3.23	3.85	3.85	2.42	2.15	3.50	3.53	
T (°C) ^c	735	748	759	750	768	770	784	804	884	932	920	830	778	899	822	
P (kbar) ^c	1.62	1.58	1.27	1.44	1.94	1.62	1.43	1.21	-	-	-	0.72	1.63	-	2.05	
FeO _{melt}	4.54	4.54	4.54	4.54	4.54	4.54	4.54	4.54	4.54	4.54	4.54	4.54	4.54	4.54	4.54	
MgO _{melt}	2.82	2.82	2.82	2.82	2.82	2.82	2.82	2.82	2.82	2.82	2.82	2.82	2.82	2.82	2.82	
K _D (Fe-Mg) _{Amp-melt}	0.45	0.45	0.44	0.44	0.51	0.47	0.51	0.52	0.56	0.59	0.59	0.50	0.47	0.58	0.54	
Intrusive phase	Granodiorite															
SiO ₂	45.29	46.37	48.74	46.83	47.75	44.97	44.11	45.66	48.58	48.77	46.78	47.76	49.89	49.97	50.16	
TiO ₂	2.86	2.31	1.70	2.00	2.00	2.59	2.82	2.58	1.65	1.70	2.21	2.00	0.93	0.97	0.96	
Al ₂ O ₃	9.43	8.70	7.21	8.03	7.54	9.50	10.16	9.13	7.11	6.76	8.15	7.72	4.33	4.29	4.34	
FeO	13.43	12.61	12.66	13.59	12.82	13.88	14.15	13.76	12.70	12.17	12.61	12.72	10.86	10.87	10.93	
MnO	0.20	0.23	0.38	0.21	0.36	0.47	0.34	0.24	0.28	0.18	0.28	0.45	0.39	0.39	0.40	
MgO	12.64	12.94	13.14	12.22	13.12	11.99	11.46	12.19	13.49	13.72	12.79	13.28	15.40	15.41	16.00	
CaO	10.93	11.36	11.48	11.11	11.02	11.25	11.40	11.65	11.05	11.26	11.49	11.12	11.70	11.71	11.87	
Na ₂ O	1.92	1.84	1.67	1.98	1.85	2.07	2.10	2.06	1.74	1.71	2.00	1.78	2.03	1.81	1.08	
K ₂ O	0.91	0.75	0.59	0.70	0.71	0.79	0.84	0.76	0.60	0.57	0.72	0.65	0.68	0.69	0.46	
Total	97.63	97.15	97.60	96.73	97.19	97.55	97.54	98.17	97.23	96.88	97.03	97.53	96.40	96.40	96.33	
Si	6.68	6.83	7.11	6.95	7.02	6.67	6.56	6.72	7.11	7.15	6.90	6.99	7.34	7.35	7.35	
Al ^{IV}	1.32	1.17	0.89	1.05	0.98	1.33	1.44	1.28	0.89	0.85	1.10	1.01	0.66	0.65	0.65	
Al ^{VI}	0.32	0.34	0.35	0.36	0.32	0.33	0.34	0.30	0.34	0.31	0.32	0.32	0.09	0.09	0.10	
Ti	0.32	0.26	0.19	0.22	0.22	0.29	0.32	0.28	0.18	0.19	0.25	0.22	0.10	0.11	0.11	
Fe ³⁺	0.34	0.23	0.16	0.18	0.25	0.27	0.22	0.17	0.27	0.21	0.13	0.28	0.13	0.16	0.28	
Fe ²⁺	1.30	1.36	1.43	1.55	1.34	1.47	1.57	1.57	1.29	1.32	1.49	1.28	1.26	1.22	1.03	
Mn	0.02	0.03	0.05	0.03	0.04	0.06	0.04	0.03	0.04	0.02	0.03	0.06	0.05	0.05	0.05	
Mg	2.78	2.84	2.86	2.70	2.88	2.65	2.54	2.67	2.94	3.00	2.81	2.90	3.38	3.38	3.50	
Ca	1.73	1.79	1.79	1.77	1.74	1.79	1.82	1.84	1.73	1.77	1.82	1.74	1.84	1.84	1.86	
Na	0.55	0.52	0.47	0.57	0.53	0.59	0.60	0.59	0.49	0.49	0.57	0.50	0.58	0.52	0.31	
K	0.17	0.14	0.11	0.13	0.13	0.15	0.16	0.14	0.11	0.11	0.14	0.12	0.13	0.13	0.09	
T (°C) ^a	867	846	792	818	806	872	892	865	788	785	834	812	755	751	748	
P (kbar) ^a	1.99	1.68	1.14	1.45	1.25	2.07	2.48	1.87	1.11	1.03	1.48	1.29	0.57	0.56	0.56	
H ₂ O _{melt} (wt.%)	4.95	5.36	5.50	5.37	4.90	5.52	5.85	5.38	5.06	4.91	5.13	5.14	2.25	2.40	3.40	
logfO ₂	-12.08	-12.35	-13.26	-13.05	-12.97	-12.21	-12.10	-12.37	-13.13	-13.18	-12.67	-12.80	-13.23	-13.26	-12.97	
ΔNNO	0.41	0.55	0.76	0.42	0.75	0.18	-0.10	0.17	0.98	1.00	0.46	0.80	1.66	1.70	2.07	
T (°C) ^b	872	849	800	825	819	870	886	865	801	800	843	822	785	778	756	
P (kbar) ^b	3.43	2.91	1.96	2.52	2.17	3.52	4.05	3.19	1.91	1.73	2.56	2.26	0.71	0.70	0.71	
T (°C) ^c	927	854	770	814	811	892	925	888	764	771	840	810	669	675	672	
P (kbar) ^c	-	0.60	1.59	1.25	0.94	-	-	-	1.62	1.25	0.65	1.04	0.64	0.57	0.59	
FeO _{melt}	4.54	4.54	4.54	4.54	4.54	4.54	4.54	4.54	4.54	4.54	4.54	4.54	4.54	4.54	4.54	
MgO _{melt}	2.82	2.82	2.82	2.82	2.82	2.82	2.82	2.82	2.82	2.82	2.82	2.82	2.82	2.82	2.82	
K _D (Fe-Mg) _{Amp-melt}	0.54	0.49	0.49	0.56	0.49	0.58	0.62	0.57	0.47	0.45	0.50	0.48	0.36	0.36	0.34	
Intrusive phase Diorite porphyry																
SiO ₂	48.33	47.41	47.81	47.76	48.20	46.59	45.32	45.49	46.22	45.75	45.44	45.49	45.82	45.63	46.51	46.30

Table 4 (continued)

Intrusive phase Diorite porphyry																
TiO ₂	1.61	1.84	1.44	1.71	1.64	2.38	2.38	2.21	2.16	2.01	1.95	2.39	2.05	2.02	1.82	1.74
Al ₂ O ₃	6.70	7.69	6.67	6.72	6.48	8.56	9.07	8.87	8.10	8.83	9.05	8.91	7.92	7.89	7.49	7.05
FeO	12.61	12.62	12.76	12.45	12.48	13.02	12.97	12.93	12.89	13.31	13.92	14.10	13.16	12.95	13.30	13.51
MnO	0.39	0.35	0.29	0.47	0.35	0.29	0.39	0.23	0.41	0.41	0.31	0.38	0.38	0.34	0.45	0.41
MgO	13.88	13.62	13.68	13.65	13.87	12.74	12.56	12.83	13.18	12.32	12.19	12.07	13.29	13.47	13.41	13.62
CaO	11.46	11.33	11.39	11.59	11.48	11.10	11.06	11.09	11.17	11.24	11.11	11.22	11.17	11.43	11.51	11.27
Na ₂ O	1.34	1.52	1.34	1.26	1.32	1.69	1.69	1.76	1.72	1.77	1.65	1.63	1.66	1.62	1.55	1.49
K ₂ O	0.71	0.77	0.58	0.58	0.61	0.82	0.92	0.84	0.69	0.87	0.77	0.76	0.85	0.87	0.69	0.72
Total	97.02	97.18	96.01	96.20	96.46	97.19	96.39	96.31	96.56	96.61	96.45	97.00	96.33	96.27	96.81	96.13
Si	7.10	6.97	7.10	7.08	7.12	6.87	6.76	6.78	6.86	6.81	6.79	6.77	6.84	6.82	6.91	6.93
Al ^{IV}	0.90	1.03	0.90	0.92	0.88	1.13	1.24	1.22	1.14	1.19	1.21	1.23	1.16	1.18	1.09	1.07
Al ^{VI}	0.26	0.30	0.27	0.25	0.25	0.35	0.35	0.34	0.28	0.36	0.38	0.33	0.24	0.21	0.22	0.17
Ti	0.18	0.20	0.16	0.19	0.18	0.26	0.27	0.25	0.24	0.23	0.22	0.27	0.23	0.23	0.20	0.20
Fe ³⁺	0.32	0.33	0.33	0.29	0.30	0.27	0.31	0.32	0.34	0.26	0.35	0.32	0.38	0.36	0.37	0.45
Fe ²⁺	1.23	1.22	1.25	1.26	1.24	1.34	1.30	1.29	1.25	1.41	1.37	1.43	1.23	1.24	1.27	1.20
Mn	0.05	0.04	0.04	0.06	0.04	0.04	0.05	0.03	0.05	0.05	0.04	0.05	0.05	0.04	0.06	0.05
Mg	3.04	2.99	3.03	3.02	3.05	2.80	2.79	2.85	2.92	2.74	2.72	2.68	2.96	3.00	2.97	3.04
Ca	1.80	1.78	1.81	1.84	1.82	1.75	1.77	1.77	1.78	1.79	1.78	1.79	1.79	1.83	1.83	1.81
Na	0.38	0.43	0.39	0.36	0.38	0.48	0.49	0.51	0.50	0.51	0.48	0.47	0.48	0.47	0.45	0.43
K	0.13	0.15	0.11	0.11	0.11	0.15	0.17	0.16	0.13	0.16	0.15	0.14	0.16	0.17	0.13	0.14
T (°C) ^a	790	817	789	796	787	835	856	852	835	846	847	848	836	843	825	816
P (kbar) ^a	1.01	1.29	1.02	1.03	0.96	1.61	1.87	1.78	1.45	1.77	1.87	1.79	1.40	1.40	1.25	1.12
H ₂ O _{melt} (wt.%)	4.62	4.82	4.94	5.03	4.71	5.30	5.25	5.16	5.00	5.44	5.88	5.71	4.33	4.16	4.65	4.11
logfO ₂	-12.88	-12.49	-12.88	-12.85	-12.95	-12.57	-12.17	-12.13	-12.33	-12.41	-12.33	-12.47	-12.19	-12.02	-12.35	-12.34
ΔNNO	1.18	1.01	1.21	1.10	1.19	0.55	0.52	0.65	0.79	0.48	0.55	0.38	0.91	0.95	0.98	1.18
T (°C) ^b	790	816	786	793	789	838	853	850	837	840	833	840	834	837	818	810
P (kbar) ^b	1.71	2.26	1.74	1.75	1.62	2.82	3.24	3.09	2.56	3.07	3.24	3.11	2.47	2.46	2.19	1.97
FeO _{melt}	4.50	4.50	4.50	4.50	4.50	4.50	4.50	4.50	4.50	4.50	4.50	4.50	4.50	4.50	4.50	4.50
MgO _{melt}	1.85	1.85	1.85	1.85	1.85	1.85	1.85	1.85	1.85	1.85	1.85	1.85	1.85	1.85	1.85	1.85
K _D (Fe-Mg) ^{Amp-melt}	0.52	0.53	0.54	0.52	0.52	0.59	0.59	0.58	0.56	0.62	0.66	0.67	0.57	0.55	0.57	0.57
Intrusive phase	Diorite porphyry															
SiO ₂	46.99	46.61	47.20	46.26	47.04	48.09	48.79	48.54	45.19	46.22	46.98	45.97	48.55	42.90	46.99	
TiO ₂	1.90	1.65	1.67	1.68	1.48	1.17	1.17	1.30	1.97	1.76	1.58	2.05	1.42	1.89	1.90	
Al ₂ O ₃	7.59	7.81	7.20	7.76	6.80	5.99	5.35	5.82	8.01	7.65	6.95	7.51	6.78	10.96	7.59	
FeO	13.15	13.12	12.90	13.17	13.07	12.93	11.83	12.26	13.45	12.81	12.67	12.80	10.38	13.11	13.15	
MnO	0.41	0.37	0.48	0.45	0.44	0.56	0.49	0.48	0.50	0.35	0.38	0.40	0.44	0.37	0.41	
MgO	13.54	13.49	13.73	13.35	13.85	14.13	15.06	14.66	13.44	13.82	13.99	13.46	15.14	12.34	13.54	
CaO	11.48	11.36	11.55	11.54	11.51	11.46	11.66	11.43	11.40	11.59	11.53	11.62	11.81	11.54	11.48	
Na ₂ O	1.55	1.67	1.46	1.61	1.33	1.11	1.10	1.34	1.68	1.52	1.39	1.50	1.27	2.00	1.55	
K ₂ O	0.78	0.70	0.69	0.68	0.66	0.62	0.59	0.56	0.91	0.78	0.60	0.74	0.58	0.69	0.78	
Total	97.42	96.79	96.88	96.52	96.18	96.06	96.03	96.40	96.57	96.52	96.11	96.07	96.55	96.20	97.42	
Si	6.87	6.92	6.91	6.98	6.89	7.01	7.15	7.22	7.17	6.76	6.87	6.99	6.87	7.10	6.45	
Al ^{IV}	1.13	1.08	1.09	1.02	1.11	0.99	0.85	0.78	0.83	1.24	1.13	1.01	1.13	0.90	1.55	
Al ^{VI}	0.14	0.24	0.27	0.23	0.25	0.21	0.20	0.15	0.18	0.18	0.22	0.21	0.20	0.27	0.40	
Ti	0.19	0.21	0.18	0.19	0.19	0.17	0.13	0.13	0.14	0.22	0.20	0.18	0.23	0.16	0.21	
Fe ³⁺	0.42	0.35	0.38	0.36	0.35	0.41	0.43	0.39	0.40	0.43	0.38	0.39	0.32	0.29	0.39	
Fe ²⁺	1.19	1.26	1.23	1.22	1.27	1.19	1.14	1.04	1.09	1.21	1.19	1.16	1.28	0.99	1.24	
Mn	0.05	0.05	0.05	0.06	0.06	0.06	0.07	0.06	0.06	0.06	0.04	0.05	0.05	0.05	0.05	
Mg	3.10	2.97	2.98	3.03	2.96	3.08	3.13	3.32	3.23	3.00	3.06	3.10	3.00	3.30	2.77	
Ca	1.86	1.81	1.80	1.83	1.84	1.84	1.83	1.85	1.81	1.83	1.85	1.84	1.86	1.85	1.86	

Table 4 (continued)

Intrusive phase	Diorite porphyry														
Na	0.45	0.44	0.48	0.42	0.47	0.38	0.32	0.32	0.38	0.49	0.44	0.40	0.43	0.36	0.58
K	0.14	0.15	0.13	0.13	0.13	0.13	0.12	0.11	0.11	0.17	0.15	0.11	0.14	0.11	0.13
T (°C) ^a	832	823	827	814	831	805	777	770	777	851	834	811	834	803	920
P (kbar) ^a	1.18	1.26	1.34	1.15	1.34	1.05	0.86	0.72	0.81	1.43	1.30	1.09	1.27	1.02	3.06
H ₂ O _{melt} (wt.%)	3.95	4.52	4.83	4.63	4.87	4.47	4.43	3.83	4.06	3.93	4.36	4.59	4.46	4.77	6.54
logfO ₂	-11.97	-12.40	-12.27	-12.45	-12.23	-12.47	-12.85	-12.76	-12.78	-11.83	-12.02	-12.36	-12.21	-12.25	-11.04
ΔNNO	1.23	0.98	1.03	1.12	0.97	1.29	1.51	1.77	1.58	0.98	1.13	1.27	0.94	1.54	0.46
T (°C) ^b	822	819	821	808	822	796	768	769	781	842	825	805	828	805	894
P (kbar) ^b	2.07	2.21	2.37	2.01	2.36	1.81	1.40	1.10	1.30	2.55	2.29	1.89	2.23	1.73	4.82
FeO _{melt}	4.50	4.50	4.50	4.50	4.50	4.50	4.50	4.50	4.50	4.50	4.50	4.50	4.50	4.50	4.50
MgO _{melt}	1.85	1.85	1.85	1.85	1.85	1.85	1.85	1.85	1.85	1.85	1.85	1.85	1.85	1.85	1.85
K _D (Fe-Mg) ^{Amp-melt}	0.54	0.56	0.56	0.54	0.57	0.54	0.53	0.45	0.48	0.58	0.53	0.52	0.55	0.39	0.61
Intrusive phase	Diorite porphyry														
SiO ₂		42.87	42.69	46.50	46.72	46.39	46.31	47.16	49.26	44.29	45.86				
TiO ₂		2.10	2.27	1.91	1.76	1.85	2.09	1.72	1.50	2.34	1.92				
Al ₂ O ₃		11.25	11.08	7.52	7.54	7.75	8.02	7.27	6.54	8.93	8.18				
FeO		11.98	12.63	13.06	12.50	13.52	13.23	13.09	11.80	13.81	13.18				
MnO		0.47	0.38	0.29	0.35	0.43	0.43	0.48	0.30	0.40	0.44				
MgO		12.92	12.54	13.50	13.67	13.00	13.09	13.30	13.66	12.58	13.22				
CaO		11.80	11.60	11.25	11.52	11.28	11.07	10.93	11.94	11.70	11.52				
Na ₂ O		2.13	1.92	1.58	1.59	1.54	1.58	1.71	1.15	1.64	1.57				
K ₂ O		0.61	0.79	0.62	0.60	0.69	0.66	0.71	0.78	0.91	0.78				
Total		96.41	96.19	96.29	96.28	96.45	96.48	96.41	96.93	96.62	96.67				
Si		6.41	6.41	6.92	6.94	6.91	6.89	7.01	7.21	6.65	6.83				
Al ^{IV}		1.59	1.59	1.08	1.06	1.09	1.11	0.99	0.79	1.35	1.17				
Al ^{VI}		0.39	0.38	0.24	0.26	0.27	0.29	0.28	0.33	0.23	0.26				
Ti		0.24	0.26	0.21	0.20	0.21	0.23	0.19	0.16	0.26	0.21				
Fe ³⁺		0.34	0.37	0.39	0.32	0.37	0.39	0.37	0.10	0.34	0.36				
Fe ²⁺		1.15	1.20	1.22	1.23	1.30	1.22	1.24	1.41	1.39	1.27				
Mn		0.06	0.05	0.04	0.04	0.05	0.05	0.06	0.04	0.05	0.06				
Mg		2.88	2.81	3.00	3.03	2.89	2.90	2.94	2.98	2.81	2.93				
Ca		1.89	1.87	1.79	1.83	1.80	1.76	1.74	1.87	1.88	1.84				
Na		0.62	0.56	0.46	0.46	0.44	0.45	0.49	0.33	0.48	0.45				
K		0.12	0.15	0.12	0.11	0.13	0.12	0.13	0.14	0.17	0.15				
T (°C) ^a		938	930	821	824	822	827	805	779	875	843				
P (kbar) ^a		3.25	3.15	1.26	1.27	1.34	1.42	1.18	0.98	1.83	1.49				
H ₂ O _{melt} (wt.%)		6.57	6.23	4.79	4.96	5.07	5.19	4.63	5.10	4.77	4.86				
logfO ₂		-10.70	-10.90	-12.39	-12.31	-12.51	-12.43	-12.76	-13.30	-11.80	-12.09				
ΔNNO		0.49	0.42	1.02	1.04	0.87	0.85	0.99	1.01	0.54	0.87				
T (°C) ^b		917	906	821	822	816	826	810	777	858	832				
P (kbar) ^b		5.02	4.92	2.21	2.22	2.36	2.51	2.06	1.62	3.18	2.62				
FeO _{melt}		4.50	4.50	4.50	4.50	4.50	4.50	4.50	4.50	4.50	4.50				
MgO _{melt}		1.85	1.85	1.85	1.85	1.85	1.85	1.85	1.85	1.85	1.85				
K _D (Fe-Mg) ^{Amp-melt}		0.53	0.58	0.56	0.53	0.60	0.58	0.57	0.50	0.63	0.57				

Note: the structural formulae of the amphibole were calculated on the basis of 23 oxygen atoms

^aTemperature and pressure values are calculated using the Al-in-amphibole thermobarometry (Ridolfi and Renzulli 2012)

^bTemperature and pressure values are calculated using the Si-in-amphibole thermobarometry (Putirka 2016)

^cTemperature and pressure values are calculated using the amphibole thermobarometry (Anderson and Smith 1995)

FeO_{melt} and MgO_{melt} contents from Liu et al. (2021). “-”: No data obtained

Acknowledgements Dante Canil and Gordon Moore are thanked for reviewing and handling and Constantinos Mavrogonatos for a detailed and thoughtful review, which greatly improved the manuscript. We are grateful to Yuedong Pan, Quanzeng Li, and, Zhikai Xu during field work. This study was financially supported by the China Postdoctoral Science Foundation (2022M721304) to Y Liu and the National Natural Science Foundation of China project (42072085) and the National Key Research and Development Program of China (2017YFC0601306) to JG Sun. Yang Liu was funded by the China Scholarship Council. The University of Melbourne thermochronology laboratory receives support under the AuScope program of the National Collaborative Research Infrastructure Strategy (NCRIS).

Funding This study was funded by China Postdoctoral Science Foundation (2022M721304), National Natural Science Foundation of China project (42072085), National Key Research and Development Program of China (2017YFC0601306).

Data availability The authors confirm that the data supporting the findings in this study are available within the manuscript. Samples are housed in the College of Earth Sciences at the Jilin University.

Declarations

Conflict of interest The authors declare that they have no competing financial interests or personal relationships.

References

- Alonso-Perez R, Müntener O, Ulmer P (2009) Igneous garnet and amphibole fractionation in the roots of island arcs: experimental constraints on andesitic liquids. *Contrib Mineral Petrol* 157:541
- Anderson JL, Smith DR (1995) The effects of temperature and f_{O_2} on the Al-in-hornblende barometer. *Am Mineral* 80:549–559
- Anderson JL, Barth AP, Wooden JL, Mazdab F (2008) Thermometers and thermobarometers in granitic systems. *Rev Mineral Geochem* 69:121–142
- Audétat A, Pettke T (2006) Evolution of a porphyry-Cu mineralized magma system at Santa Rita, New Mexico (USA). *J Petrol* 47:2021–2046
- Ballard JR, Palin JM, Campbell IH (2002) Relative oxidation states of magmas inferred from Ce(IV)/Ce(III) in zircon: application to porphyry copper deposits of northern Chile. *Contrib Mineral Petrol* 144:347–364
- Beucher R, Brown RW, Roper S, Stuart F, Persano C (2013) Natural age dispersion arising from the analysis of broken crystals: Part II. Practical application to apatite (U-Th)/He thermochronometry. *Geochim Cosmochim Acta* 120:395–416
- Botcharnikov RE, Holtz F, Behrens H (2015) Solubility and fluid-melt partitioning of H_2O and Cl in andesitic magmas as a function of pressure between 50 and 500 MPa. *Chem Geol* 418:117–131
- Burnham AD, Berry AJ, Halse HR, Schofield PF, Cibin G, Mosselmans JFM (2015) The oxidation state of europium in silicate melts as a function of oxygen fugacity, composition and temperature. *Chem Geol* 411:248–259
- Burrows DR, Rennison M, Burt D, Davie R (2020) The Onto Cu-Au discovery, Eastern Sumbawa, Indonesia: a large, Middle Pleistocene lithocap-hosted high-sulfidation covellite-pyrite porphyry deposit. *Econ Geol* 115:1385–1412
- Candela PA (1986) The evolution of aqueous vapor from the silicate melts: effect on oxygen fugacity. *Geochim Cosmochim Acta* 50:1205–1211
- Cao MJ, Hollings P, Cooke DR, Evans NJ, McInnes BIA, Qin KZ, Li GM, Sweet G, Baker M (2018) Physicochemical processes in the magma chamber under the Black Mountain porphyry Cu–Au deposit, Philippines: insights from mineral chemistry and implications for mineralization. *Econ Geol* 113:63–82
- Cao HH (2010) Chronology and geochemistry of Late Hercynian gabbro and diorite in Hunchun Area. PhD. Thesis, Jilin University (**in Chinese with English abstract**)
- Chai P, Sun JG, Xing SW, Men LJ, Han JL (2015) Early cretaceous arc magmatism and high-sulphidation epithermal porphyry Cu–Au mineralization in Yanbian area, Northeast China: the Duhuangling example. *Int Geol Rev* 57:1267–1293
- Chang ZS, Hedenquist JW, White NC, Cooke DR, Roach M, Deyell CL, Garcia J, Gemmill JB, McKnight S, Cuisson AL (2011) Exploration tools for linked porphyry and epithermal deposits: Example from the Mankayan intrusion-centered Cu–Au district, Luzon, Philippines. *Econ Geol* 106:1365–1398
- Chen J, Cooke DR, Piquer J, Selley D, Zhang LJ, White NC (2019) Hydrothermal alteration, mineralization, and structural geology of the Zijinshan high-sulfidation Au–Cu deposit, Fujian Province, Southeast China. *Econ Geol* 114:639–661
- Chiaradia M (2022) Distinct magma evolution processes control the formation of porphyry Cu–Au deposits in thin and thick arcs. *Earth Planet Sci Lett* 509:117864
- Chiaradia M, Caricchi L (2017) Stochastic modelling of deep magmatic controls on porphyry copper deposit endowment. *Sci Rep* 7:1–11
- Cocker HA, Valente DL, Park JW, Campbell IH (2016) Using platinum group elements to identify sulfide saturation in a porphyry Cu system: the El Abra porphyry Cu deposit, Northern Chile. *J Petrol* 56:2491–2514
- Cooke DR, Hollings P, Walshe JL (2006) Tectonic triggers for giant porphyry and epithermal deposits of the circum-Pacific region. *Geochim Cosmochim Acta* 70:A110–A110
- Dahlström SIR, Cooper FJ, Blundy J, Tapster S, Cortés Yáñez J, Evenstar LA (2022) Pluton Exhumation in the Precordillera of Northern Chile (17.8°–24.2°S): implications for the formation, enrichment, and preservation of porphyry copper deposits. *Econ Geol* 117:1043–1071
- Danišik M, McInnes BIA, Kirkland CL, McDonald BJ, Evans NJ, Becker T (2017) Seeing is believing: Visualization of He distribution in zircon and implications for thermal history reconstruction on single crystals. *Sci Adv* 3:e1601121
- Dilles JH, Kent AJR, Wooden JL, Tosdal RM, Koleszar A, Lee RG, Farmer LP (2015) Zircon compositional evidence for sulfur-degassing from ore-forming arc magmas. *Econ Geol* 110:241–251
- Du JG, Audétat A (2020) Early sulfide saturation is not detrimental to porphyry Cu–Au formation. *Geology* 48:519–524
- Eaton PC, Setterfield TN (1993) The relationship between epithermal and porphyry hydrothermal systems within the Tavua caldera, Fiji. *Econ Geol* 88:1053–1083
- Evans KA, Tomkins AG (2011) The relationship between subduction zone redox budget and arc magma fertility. *Earth Planet Sci Lett* 308:401–409
- Farley K, Wolf R, Silver L (1996) The effects of long alpha-stopping distances on (U-Th)/He ages. *Geochim Cosmochim Acta* 60:4223–4229
- Farley K, Stockli DF (2002) (U-Th)/He dating of phosphates: Apatite, monazite, and xenotime. *Rev Mineral Geochem* 48:559–577
- Foley FV, Pearson NJ, Rushmer T, Turner S, Adam J (2013) Magmatic evolution and magma mixing of Quaternary adakites at Solander and Little Solander Islands, New Zealand. *J Petrol* 54:703–744

- Fu FQ, McInnes BIA, Evans NJ, Davies PJ (2010) Numerical modeling of magmatic-hydrothermal systems constrained by U-Th-Pb-He time-temperature histories. *J of Geochem Explor* 106:90–109
- Gallagher K, Brown R, Johnson C (1998) Fission track analysis and its applications to geological problems. *Annu Rev Earth Planet Sci Lett* 26:519–572
- Garwin SL (2000) The setting, geometry and timing of intrusion-related hydrothermal systems in the vicinity of the Batu Hijau porphyry copper-gold deposit, Sumbawa, Indonesia. PhD Thesis, University of Western Australia, Nedlands, Western Australia
- Gleadow AJW, Duddy IR, Green PF, Lovering JF (1986) Confined fission track lengths in apatite: a diagnostic tool for thermal history analysis. *Contrib Mineral Petrol* 94:405–415
- Gleadow A, Harrison M, Kohn B, Lugo-Zazueta R, Phillips D (2015) The Fish Canyon tuff: a new look at an old low-temperature thermochronology standard. *Earth Planet Sci Lett* 424:95–108
- Gong L, Kohn BP, Zhang ZY, Xiao B, Wu L, Chen HY (2021) Exhumation and preservation of paleozoic porphyry Cu deposits: insights from the Yandong Deposit, Southern Central Asian Orogenic Belt. *Econ Geol* 116:607–628
- Gu AL, Men LJ, Sun JG, Nagao K, Zhu JQ (2016) Origin and evolution of ore fluids in the late Mesozoic Naozhi epithermal Au–Cu deposit, Yanbian area, Northeast China: evidence from fluid inclusion and isotopic geochemistry. *Arab J Geosci* 9:117
- Guenther WR, Reiners PW, Ketcham RA, Nasdala L, Giester G (2013) Helium diffusion in natural zircon: radiation damage, anisotropy, and the interpretation of zircon (U-Th)/He thermochronology. *Am J Sci* 313:145–198
- Halter WE, Heinrich CA, Pettke T (2005) Magma evolution and the formation of porphyry Cu–Au ore fluids: evidence from silicate and sulfide melt inclusions. *Miner Deposita* 39:845–863
- Han SJ, Sun JG, Bai LA, Xing SW, Chai P, Zhang Y, Yang F, Men LJ, Li YX (2013) Geology and ages of porphyry and medium- to high-sulphidation epithermal gold deposits of the continental margin of Northeast China. *Int Geol Rev* 55:287–310
- Hao HD, Campbell IH, Park JW, Cooke DR (2017) Platinum-group element geochemistry used to determine Cu and Au fertility in the Northparkes igneous suites, New South Wales, Australia. *Geochim Cosmochim Acta* 216:372–392
- Hattori K, Keith JD (2001) Contribution of mafic melt to porphyry copper mineralization, evidence from Mount Pinatubo, Philippines, and Bingham canyon, Utah, USA. *Miner Deposita* 36:799–806
- Hedenquist JW, Arribas A, Urien-Gonzalez E (2000) Exploration for epithermal gold deposits. In: Hagemann SG, Brown PE (Eds.), *Gold in 2000*. *Rev Econ Geol* 13: 245–277
- Hollings P, Cooke DR (2005) Regional geochemistry of Tertiary igneous rocks in Central Chile: Implications for the geodynamic environment of giant porphyry copper and epithermal gold mineralization. *Econ Geol* 100:887–904
- Hollings P, Sweet G, Baker M, Cooke DR, Fiedman R (2013) Tectonomagmatic controls on porphyry mineralization: geochemical evidence from the Black Mountain porphyry system, Philippines. *Soc Econ Geol Spec Publ* 17:301–335
- Holtz F, Behrens H, Dingwell DB, Johannes W (1995) H₂O solubility in haplogranitic melts: compositional, pressure, and temperature dependence. *Am Mineral* 80:94–108
- Ketcham RA, Carter A, Donelick RA, Barbarand J, Hurford AJ (2007) Improved modelling of fission-track annealing in apatite. *Am Mineral* 92:799–810
- Leake BE, Woollet AR, Arps CES, Birch WD, Gilbert MC, Grice JD, Hawthorne FC, Kato A, Kisch HJ, Krivovichev EA (1997) Nomenclature of amphiboles: report of the subcommittee on amphiboles of the International Mineralogical Association, Commission on New Minerals and Mineral Names. *Can Mineral* 35:219–246
- Leng CB, Cooke DR, Hou ZQ, Evans NJ, Zhang XC, Chen WT, Danišik M, McInnes BIA, Yang JH (2018) Quantifying exhumation at the giant Pulang porphyry Cu–Au deposit using U–Pb–He dating. *Econ Geol* 113:1077–1092
- Li XP, Sun JG, Liu Y, Wang QH, Ren ZN, Gu XL (2020) Zircon U–Pb chronology, geochemistry and geological implications of Mesozoic volcanic rocks from Naozhi copper-gold mining area, Yanbian. *Global Geology* 39:528–543 (**in Chinese with English abstract**)
- Liu Y, Zhang Y, Sun JG, Xu ZK, Liu YM, Zhang XW, Pan YD, Han JL, Chu XL (2020) Petrology, geochemistry, and zircon U–Pb isotopes of Xintian Complex in Yanbian area, Northeast China: evidence for magma mixing and geodynamics processes. *Geol J* 55:5417–5431
- Liu Y, Sun JG, Wang QH, Pan YD, Xu ZK, Lei FZ, Li XP, Zhang XW, Liu YM (2021) Petrogenesis and oxygen fugacity of the Xintian complex associated with the Naozhi–Xintian porphyry–epithermal system in the Yanbian area. *NE China Ore Geol Rev* 134:104128
- Liu Y, Hollings P, Sun JG, Brzozowski BJ (2022) Hydrothermal evolution from porphyry- to epithermal-style mineralization in the Naozhi deposit. *NE China Ore Geol Rev* 150:105131
- Liu JL, Sun FY, Lin BL, Wang G, Xu QL, Ao Z (2015) Geochronology and geochemistry of trachyandesite of Naozhi gold deposit in Yanbian region, Southern Jilin Province and its geological significance. *J. Jilin Univ. (Earth Sci. Ed.)* 45: 1394–1404 (**in Chinese with English abstract**)
- Loucks RR (2014) Distinctive composition of copper-forming arc magmas. *Aust J Earth Sci* 61:5–16
- Loucks RR, Fiorentini ML, Rohrlach BD (2018) Divergent T–fO₂ paths during crystallisation of H₂O-rich and H₂O poor magmas as recorded by Ce and U in zircon, with implications for Titaniz and Titaniz geothermometry. *Contrib Mineral Petrol* 173:104
- Lu YJ, Loucks RR, Fiorentini ML, McCuaig TC, Evans N, Yang ZM, Hou ZQ, Kirkland C, Parra-Avila LS, Kobussen A (2016) Zircon compositions as a pathfinder for porphyry Cu ± Mo ± Au deposits. *Soc Econ Geol Spec Publ* 19:329–347
- Ma XH, Zhu WP, Zhou ZH, Qiao SL (2017) Transformation from Paleo-Asian Ocean closure to Paleo-Pacific subduction: New constraints from granulites in the eastern Jilin-Heilongjiang Belt, NE China. *J Asian Earth Sci* 144:261–286
- Matjuschkina V, Blundy JD, Brooker RA (2016) The effect of pressure on sulphur speciation in mid- to deep-crustal arc magmas and implications for the formation of porphyry copper deposits. *Contrib Mineral Petrol* 171:66
- McInnes BIA, Evans NJ, Fu FQ (2005) Application of thermochronology to hydrothermal ore deposits. *Rev Mineral Geochem* 58:467–498
- Moore G, Vennemann T, Carmichael ISE (1998) An empirical model for the solubility of H₂O in magmas to 3 kilobars. *Am Mineral* 83:36–42
- Morón S, Kohn BP, Beucher R, Mackintosh V, Cawood PA, Moresi L, Gallagher SJ (2020) Denuding a craton: thermochronology record of Phanerozoic unroofing from the Pilbara Craton, Australia. *Tectonic* 39: e2019TC005988
- Muntean OL, Einaudi MT (2001) Porphyry–epithermal transition: Maricunga Belt, Northern Chile. *Econ Geol* 96:743–772
- Putirka K (2008) Thermometers and barometers for volcanic systems. *Rev Mineral Geochem* 69:61–120
- Putirka K (2016) Amphibole thermometers and barometers for igneous systems and some implications for eruption mechanisms of felsic magmas at arc volcanoes. *Am Mineral* 101:841–858
- Reiners PW (2005) Zircon (U–Th)/He Thermochronometry. *Rev Mineral Geochem* 58:151–179
- Ren YS, Chen C, Zou XT, Zhao HL, Hao YJ, Hou HN, Hu ZC, Jiang GH (2016) The age, geological setting, and types of gold deposits

- in the Yanbian and adjacent areas, NE China. *Ore Geol Rev* 73:284–297
- Richards JP (2003) Tectono–magmatic precursors for porphyry Cu–(Mo–Au) deposit formation. *Econ Geol* 98:1515–1533
- Richards JP (2011a) Magmatic to hydrothermal metal fluxes in convergent and collided margins. *Ore Geol Rev* 40:1–26
- Richards JP (2011b) High Sr/Y arc magmas and porphyry Cu ± Mo ± Au deposits: just add water. *Econ Geol* 106:1075–1081
- Ridolfi F, Renzulli A (2012) Calcic amphiboles in calc-alkaline and alkaline magmas: thermobarometric and chemometric empirical equations valid up to 1130C and 2.2 GPa. *Contrib Mineral Petrol* 163:877–895
- Ridolfi F, Renzulli A, Puerini M (2010) Stability and chemical equilibrium of amphibole in calc-alkaline magmas: an overview, new thermobarometric formulations and application to subduction-related volcanoes. *Contrib Mineral Petrol* 160:45–66
- Roedder E (1971) Fluid inclusion studies on the porphyry-type ore deposits at Bingham, Utah, Butte, Montana, and Climax, Colorado. *Econ Geol* 66:98–118
- Sato H, Nakada S, Fujii T, Nakamura M, Suzuki-Kamata K (1999) Groundmass pargasite in the 1991–1995 dacite of Unzen volcano: phase stability experiments and volcanological implications. *J Volcanol Geoth Res* 89:197–212
- Seedorff E, Dilles JH, Proffett JM Jr, Einaudi MT, Zurcher L, Stavast WJA, Johnson DA, Barton MD (2005) Porphyry deposits: characteristics and origin of hypogene features. *Econ Geol* 100:251–298
- Shi CL (2008) Cretaceous strata sequence and basin evolution of Yanji Basin. Master Thesis, Jilin University **(in Chinese with English abstract)**
- Sillitoe RH (2010) Porphyry copper systems. *Econ Geol* 150:3–41
- Sillitoe RH, Hedenquist JW (2003) Linkages between volcanotectonic settings, ore–fluid compositions, and epithermal precious–metal deposits. *Soc Econ Geol Spec Publ* 10:315–343
- Simmons SF, White NC, John DA (2005) Geological characteristics of epithermal precious and base metal deposits. *Econ Geol* 100:485–522
- Sun JG, Men LJ, Zhao JK, Chen L, Liang SN, Chen D, Feng W (2008) Zircon chronology of melanocratic dykes in the district of the Xiaoxinancha Au–rich Cu deposit in Yanbian and its geological implication. *Acta Petrol Sin* 82:517–527 **(in Chinese with English abstract)**
- Sun JG, Zhang Y, Han SJ, Men LJ, Li YX, Chai P, Yang F (2013) Timing of formation and geological setting of low–sulphidation epithermal gold deposits in the continental margin of NE China. *Int Geol Rev* 55:608–632
- Tomlinson DH Jr, Christiansen EH, Keith JD, Dorais MJ, Ganske R, Fernandez D, Vetz N, Sorensen M, Gibbs J (2021) Nature and origin of zoned polymetallic (Pb–Zn–Cu–Ag–Au) veins from the Bingham Canyon porphyry Cu–Au–Mo deposit, Utah. *Econ Geol* 116:747–771
- Wagner GA, Haute PVD (1992) Fission-track dating. Kluwer Academic, Dordrecht
- Wilde SA (2015) Final amalgamation of the Central Asian Orogenic Belt in NE China: Paleo-Asian Ocean closure versus Paleo-Pacific plate subduction—a review of the evidence. *Tectonophysics* 662:345–362
- Wilkinson JJ (2013) Triggers for the formation of porphyry ore deposits in magmatic arcs. *Nat Geosci* 6:917–925
- Wolfe MR, Stockli DF (2010) Zircon (U–Th)/He thermochronometry in the KTB drill hole, Germany, and its implications for bulk He diffusion kinetics in zircon. *Earth Planet Sci Lett* 295:69–82
- Wu FY, Sun DY, Ge WC, Zhang YB, Grant ML, Wilde SA, Jahn BM (2011) Geochronology of the Phanerozoic granitoids in northeastern China. *J Asian Earth Sci* 41:1–30
- Xu WL, Wang F, Pei FP, Meng E, Tang J, Xu MJ, Wang W (2013) Mesozoic tectonic regimes and regional ore-forming background in NE China: constrains from spatial and temporal variations of Mesozoic volcanic rock associations. *Acta Petrol Sin* 29:339–353 **(in Chinese with English abstract)**

Publisher's Note Springer Nature remains neutral with regard to jurisdictional claims in published maps and institutional affiliations.

Springer Nature or its licensor (e.g. a society or other partner) holds exclusive rights to this article under a publishing agreement with the author(s) or other rightsholder(s); author self-archiving of the accepted manuscript version of this article is solely governed by the terms of such publishing agreement and applicable law.